Post-Print

This is the accepted version of:

G. Droandi, G. Gibertini
Aerodynamic Shape Optimisation of a Proprotor and Its Validation by Means of CFD and Experiments
The Aeronautical Journal, Vol. 119, N. 1220, 2015, p. 1223-1251
doi:10.1017/S0001924000011222

The final publication is available at https://doi.org/10.1017/S0001924000011222

Aerodynamic Shape Optimisation of a Proprotor and its Validation by Means of CFD and Experiments

G.Droandi, G.Gibertini

Dipartimento di Scienze e Tecnologie Aerospaziali
Politecnico di Milano, Campus Bovisa, Via La Masa 34, 20156 Milano, Italy
e-mail: giovanni.droandi@polimi.it

Abstract

The aerodynamic shape design of a proprotor for a tiltrotor aircraft is a very complex and demanding task because it has to combine good hovering capabilities with high propeller efficiency. The aim of the present work is to describe a two–level procedure and its results for the aerodynamic shape design of a new rotor blade for a high–performance tiltwing tiltrotor aircraft taking into account the most important flight conditions in which the aircraft can operate. Span–wise distributions of twist, chord and airfoil were chosen making use of a multi–objective genetic optimiser that worked on three objectives simultaneously. A non–linear sweep angle distribution along the blade was designed to reduce the power losses due to compressibility effects during axial flight at high speed. During the optimisation process, the aerodynamic performance of the blade was evaluated with a classical two–dimensional strip theory solver. The optimised blade was than analysed by means of a compressible Navier–Stokes solver and calculations were validated comparing numerical results with experimental data obtained from wind tunnel tests of a scaled model of the proprotor.

Nomenclature

ASI	Airfoil Shape Index
c	Blade local chord [m]
c_∞	Free stream speed of sound [m/s]
C_P	Power coefficient, $P/(\rho\pi\Omega^3 R^5)$
C_T	Thrust coefficient, $T/(\rho\pi\Omega^2 R^4)$
FM	Figure of merit, $C_T^{3/2}/(\sqrt{2}C_P)$
Λ	Sweep angle [deg]
M_{dd}	Drag divergence Mach number
M_n	Normal Mach number
M_{Tip}	Blade tip Mach number
M_∞	Free stream Mach number
M_t	Blade aerodynamic torsional moment [Nm]
n	Rotor angular speed [rps]
N_b	Number of blades
η_{climb}	Propulsive efficiency in climb, (TV_{climb}/P)
η_{cruise}	Propulsive efficiency in cruise, (TV_{cruise}/P)
Ω	Angular speed [rad/s]
P	Rotor power [Nm/s]
R	Rotor radius [m]
r	Radial distance (from rotor axis) [m]
ρ	Air density [kg/m^3]
σ	Rotor solidity, $cN_b/(\pi R)$
σ_M	Aerodynamic torsional moment standard deviation
T	Rotor thrust [N]
T_r	Required rotor thrust [N]
θ_0	Rotor trim pitch angle [deg]
θ	Blade local pitch angle [deg]
U_P	Resultant local axial velocity [m/s]
U_T	Resultant local azimuthal velocity [m/s]
V_{climb}	Free stream velocity in climbing flight [m/s]
V_{cruise}	Free stream velocity in cruise flight [m/s]
ζ	Sectional displacement [m]
$\mathbf{x}$	Variables array

1 Introduction

After over five year decades, tiltrotor aircraft have nowadays become a reality in the modern rotorcraft scenario, combining the advantages and the peculiarities of helicopters together with modern propeller aircraft and representing a concrete possibility to overcome the main limitations of them both [1]. The capabilities of vertical take–off and landing and of high speed cruise flight are allowed by one [2] or two [3] pairs of tilting rotors (commonly called proprotors) that are employed to provide the correct amount of lift in helicopter flight mode and of thrust in aeroplane flight mode. Thanks to their high versatility [4], tiltrotor aircraft have the capability to fulfil civil roles representing nowadays a very attractive compromise for the civil industry [5]. However it is well known that the conventional design of tiltrotor leads to some important limitations in terms of aircraft performance. For instance, the aerodynamic interaction which occurs in helicopter mode between wing and rotors negatively impacts on the hovering performance of the aircraft [6]. Since a huge portion of the wing is immersed in the rotor slipstream, a non–negligible aerodynamic force [7, 8] is generated on the wing in the opposite direction of the rotor thrust (download). In order to guarantee acceptable hover performance and to balance both the aircraft weight and the aerodynamic force acting on the wing, large rotors were adopted on conventional tiltrotor (XV–15, V–22 Osprey and BA609). However, this solution leads to some important drawbacks. For instance, huge rotor dimensions prevent the take–off and landing in aeroplane mode and negatively impact on the propeller efficiency in cruise flight at high speed. Propeller efficiency limitation increases the fuel consumption and consequently decreases the aircraft operative range.

The aerodynamic design of a proprotor represents a significant challenge in the field of tiltrotor aircraft design. Indeed, while the rotor inflow and the thrust requirement change for each achievable flight condition, a proprotor has to combine good hovering capabilities with high propeller efficiency. In the past, aerodynamic proprotor blade design for conventional tiltrotors was approached with different design methodologies. An example is represented by the procedure used by McVeigh et al. [9] who designed the XV–15 advanced composite replacement blades by first determining the shapes that are ideal for each flight condition and then developing an intermediate planform and twist distribution that gives acceptable hover and cruise performance. By following a similar approach, a civil derivative of the V–22 Osprey tiltrotor was investigated by Paisley [10] who carried out an aerodynamic blade shape optimisation to improve the cruise speed of the aircraft. In order to have an acceptable compromise between hover and cruise performance, a more sophisticated closed–loop numerical optimisation procedure employing non–linear programming techniques was proposed by Liu et al. [11].

With the aim of improving the performance of the aircraft in aeroplane mode (i.e. the maximum cruise speed reachable and the aircraft operative range) non conventional tiltrotor configurations were studied over the years. An interesting and promising solution is represented by the tiltwing concept proposed for the first time by the Vertol Division of Boeing with the VZ–2 (or Model 76) tiltwing research vehicle [12]. The capability of the VZ–2 to rotate the whole wing together with the aircraft propulsive units resulted in a significant download reduction, allowing the use of two small, three–bladed propellers instead of helicopter–like rotors with huge diameters. The tiltwing concept was re–introduced in the frame of the research project ERICA (Enhanced Rotorcraft Innovative Concept Achievement [13]) funded by the European Community at the beginning of 2000s. ERICA has the capability to rotate the rotor and the outer wing portion, that is completely immersed in the rotor wake flow. The main effect of the outer wing portion rotation is the alleviation of the wing download that allows to significantly reduce the rotor radius, increasing the aircraft performance in cruise at high–speed and permitting horizontal take–off and landing. A description of the computational methods involved in the aerodynamic and aeroacoustic optimisation of the ERICA rotor blade was reported by Lefebvre et al. [14]. Different blade shapes were analysed by Beaumier et al. [15], who also compared numerical predictions and experimental data. Note that all the analysed blade shapes for the ERICA rotor are more similar to the turboprop rotor than to conventional proprotors.

In general, the aerodynamic design of a rotor blade is a very complex task. Apart from the choice of appropriate chord, twist and airfoil distributions along the blade span, as discussed by Leishman and Rosen [16], the blade tip shape and the sweep angle distributions play an important role to increase the rotor performance in aeroplane mode. An extensive description of the rotor blade tip design technologies for the improvement of helicopter performance was given by Brocklehurst and Barakos [17], while a simple method to account for the sweep angle distribution in the proprotor blade design was described by Liu and McVeigh [18]. Other important aspects in the frame of rotor blade design are represented by blade deformation, aeroelastic effects and dynamic considerations. As discussed by Le Pape and Beaumier [19], these aspects should not be completely avoided. However, appropriate coupling strategies between aerodynamic and structural solvers, needed for example in the evaluation of aerodynamic performance in forward flight [20], usually requir a huge amount of computations that do not properly fit with optimisation procedures. Since only axial flight conditions were considered in the present work, aeroelastic effects and blade deformations were not accounted during the optimisation process.

In order to ensure good performance over the entire flight envelope, during the proprotor design process it is crucial to take into account at least the most important flight conditions in which the

aircraft can operate. Since they could be very different from each other, the aerodynamic design of a proprotor blade can be seen like a shape optimisation problem characterised by multiple objectives and, in general, can be approached in two different ways. If the objectives are combined together using weighting coefficients, a multi–objective optimisation problem can be considered as a single–objective optimisation problem [21]. In practice, the problem concerns the proper choice of the weights but this operation could be non trivial and depends on the problem itself. This approach was used by Imiela [22] in a gradient–based algorithm for the optimisation of the twist rate of the 7A rotor. However, since gradient–based methods reach the nearest local optimum because of their deterministic nature, a more general optimisation technique should be used in order to ensure the achievement of the global optimum. In this regard, the development of new non–deterministic methods as genetic algorithms [23] allows to study multi–objective optimisation problems in more efficient ways. An example of a multi–objective optimisation performed by means of a genetic algorithm is presented by Leusink et al. [24] who optimised the twist and chord distributions of the 7A rotor for hover and forward flight conditions.

The use of genetic algorithms implies extremely high computational costs, especially when the genetic optimiser is coupled with a high–fidelity aerodynamic solver. Surrogate models can be used to limit the number of full cost function evaluations required to find optimal solutions, as shown by Leusink et al. [24]. A surrogate model based on artificial neural networks was recently employed by Johnson and Barakos [25] to design the anhedral and sweep distributions of the UH60–A rotor blade in forward flight while the Kriging technique was used by Roca León et al. [26] to build the surrogate model for the optimisation of twist, chord and sweep laws of the ERATO blade in forward flight with multiple Nash Games. The Kriging method was also adopted by Wilke [27] to perform optimisation of rotor blades using variable fidelity methods.

In the present work, a two–level approach for the aerodynamic shape design of a rotor blade of a tiltwing tiltrotor aircraft [28] is described. The twist, the chord and the airfoil distributions along the blade were chosen by making use of a multi–objective genetic optimiser which worked on three objectives simultaneously. To improve the rotor performance in aeroplane mode by reducing power losses due to onset of compressibility effects, the normal Mach number criterion was used to modify the blade tip. A non–linear sweep distribution was then computed to balance the aerodynamic torsional moment around the feathering axis of the blade. To limit the computational time during the shape optimisation process, the rotor performance was computed by means of a simple aerodynamic solver based on the strip theory. Hence, more accurate calculations were carried out with the Computational Fluid Dynamics (CFD) code ROSITA (ROtorcraft Software ITAly), a Reynolds Averaged Navier–

Stokes (RANS) equations solver coupled with the one–equation turbulence model of Spalart–Allmaras and developed at Department of Aerospace Science and Technology (DAER) of Politecnico di Milano. The CFD code was used to verify the strip theory predictions and to evaluate the effects of the sweep angle on blade performance. Calculations were also validated comparing numerical results with experimental data obtained from whirl–tower tests of a 1/4–scaled model of the rotor.

2 Numerical tools

2.1 Multi–objective genetic algorithm

Since a proprotor has the capability of alternatively flying as a helicopter and as an aeroplane, a proprotor blade should be properly designed in order to satisfy several requirements which in general are very different from each other. Different aircraft flight conditions, which imply different rotor inflow and operative conditions, lead to the definition of an aerodynamic blade shape optimisation problem characterised by multiple objectives. However, since the objectives may be in conflict with each other, simultaneous optimisation of each objective is prevented [21]. In the present work the rotor blade design problem was approached by making use of a multi–objective optimisation technique in order to determine a set of optimal solutions approximating the Pareto–Optimal Front. The optimisation technique here adopted was based on the fast non–dominated sorting genetic algorithm (NSGA–II) [29] that determined the minimum of a multicomponent objective function using genetic algorithm. To move from one generation to the following ensuring elitism, the NSGA–II algorithm adopted a fast non–dominated sorting procedure to rank a population (obtained combining together the parent and its offspring population). The population reduction phase was then carried out by means of a crowded comparison operator based on the crowding–distance sorting procedure, which assured the diversity among non–dominated solutions. Scattered crossover [30], adaptive non–uniform mutation [31] and binary tournament selection operators were used to create the new offspring population. To avoid premature algorithm convergence and lack of genetic information, a well–distributed initial population was created by selecting the best individuals included in the final population given by single–objective genetic optimisations carried out previously on each objective. Further details on the implementation of the multi–objective optimiser can be found in the paper by Droandi and Gibertini [32] and in Droandi's doctoral dissertation [33].

The present study used a modified implementation of the NSGA–II algorithm included in the Global Optimisation Toolbox [34] of Matlab®. The computational time of the optimisation was significantly reduced by using the parallel computing environment provided by the Parallel Computing

Toolbox [35] of Matlab®, which allowed the code to run in parallel during the fitness function evaluation. The optimisation process was carried out on a computer made up of a bi–processor quad–core Intel® Xeon® CPU E5405 at 2.00 GHz.

2.2 BEMT solver

The use of a genetic algorithm implied a huge number of fitness function evaluations in the optimisation procedure. Moreover, every time the fitness function was evaluated, the aerodynamic performance of a blade needed to be computed as many times as the number of flight conditions considered. Given that CFD computations are very time consuming, to reduce the computational cost of the whole process, the multi–objective optimiser was coupled with an aerodynamic solver based on the classical Blade Element Momentum Theory (BEMT) approach [36, 37]. Even though this aerodynamic model is very simple, it is mathematically parsimonious [16] and suitable to predict reasonably well the performance of helicopter rotor [33], aircraft propeller [38] and proprotor [11].

It is known that the BEMT aerodynamic solver employed a physicomathematical rotor model which is based on a combination of the simple momentum theory with the classical blade element theory. This approach, that implies the assumption of an axisymmetrical flow, can be efficiently used to predict the proprotor performance both in hovering and in axial flight. In order to improve results quality swirl velocity effects [36] were also taken into account and, furthermore, the Prandtl's tip loss correction [39] was applied.

The airfoil data necessary to the BEMT solver were previously stored in tables for a wide range of angles of attack, Reynolds and Mach numbers, combining wind tunnel data [40] and two–dimensional CFD results.

2.3 CFD solver

The CFD code ROSITA [41] numerically integrates the unsteady RANS equations coupled with the one–equation turbulence model of Spalart–Allmaras [42]. Multiple moving multi–block grids can be used to form an overset grid system by means of the Chimera technique. To allow for the solution of the flow field in overset grid systems, the Navier–Stokes equations are formulated in terms of the absolute velocity, expressed in a relative frame of reference linked to each component grid. The equations are discretised in space by means of a cell–centred finite–volume implementation of Roe's scheme [43]. Second order accuracy is obtained through the use of MUSCL extrapolation supplemented with a modified version of the Van Albada limiter introduced by Venkatakrishnan [44]. The viscous terms are computed by applying Gauss' theorem and using a cell–centred discretisation scheme. Time advance-

ment is carried out with a dual–time formulation [45], employing a 2^{nd} order backward differentiation formula to approximate the time derivative and a fully unfactored implicit scheme in pseudo–time. The equation for the state vector in pseudo–time is non–linear and is solved by sub–iterations accounting for a stability condition, as shown by Hirsch [46] for viscous flow calculations. The generalised conjugate gradient (GCG), in conjunction with a block incomplete lower–upper preconditioner, is used to solve the resulting linear system.

The connectivity between the component grids is computed by means of the Chimera technique, following the approach proposed by Chesshire and Henshaw [47], with modifications to further improve robustness and performance. To speed up the tagging procedure, oct-tree and alternating digital tree data structures are employed.

The ROSITA solver is fully capable of running in parallel on computing clusters. The parallel algorithm is based on the message passing programming paradigm and the parallelisation strategy consists in distributing the grid blocks among the available processors. Numerical computations were carried out in the frame of the project ISCRA named IscrC_ASTRO on the Eurora cluster at CINECA, made up of 32 bi–processor eight–core Intel® Xeon® CPU E5–2658 at 2.10 GHz and 32 bi–processor eight–core Intel® Xeon® CPU E5–2687 at 3.10 GHz.

3 Design problem

A tiltwing aircraft in the same class of ERICA was considered in the present work. The aircraft was assumed to be a civil passenger transportation aircraft with a maximum transportable pay–load equal to 22 people plus luggage. The typical mission profile was identified as the point to point service (as the connection between two urban areas, two oil rigs, ect.) taken from and to vertports with the capability to takeoff and land both in helicopter and aeroplane flight modes. Mission requirements also included significant hover and near–hover duration (as for example rescue operations), the capability to maneuver at low speed and the possibility to flight in cruise at high speed. The reference full–scale aircraft geometrical dimensions, weights and general characteristics are reported in Table 1 (for further details on the full–scale aircraft see Droandi's doctoral dissertation [33]). In particular, the rotor number of blades ($N_b = 4$) and its radius ($R = 3.7\ m$) were fixed by comparison with existing tiltrotor models and were not analysed during the optimisation process. The problem of designing an efficient proprotor blade was formulated by taking into account the most important flight conditions included in the aircraft flight envelope. Both helicopter and aeroplane operative conditions were accounted for the optimisation process. In particular, the design was carried out considering the hovering and climbing phases in helicopter mode together with the cruise flight at high speed in aeroplane mode.

In helicopter mode, the rotational speed was set equal to 560 rpm both for hover and vertical climb while in aeroplane mode it was fixed at 430 rpm. Note that the rotor rotational speed, as well as the number of blades, the rotor radius and aircraft characteristics reported in Table 1 were defined on the basis of the number of passengers, using a linear regression technique [48] with respect to established tiltrotor aircraft configurations. A moderate free stream velocity $V_{climb} = 10\ m/s$ was chosen for the

Passengers	20 + luggage
Crew	2 pilots
Rotor speed (Helicopter)	560 rpm
Rotor speed (aeroplane)	430 rpm
Empty weight	7100 kg
Gross weight	11600 kg
Wing span	15.0 m
Wing root chord	3.0 m
Wing tilt section chord	2.5 m
Wing tip chord	2.0 m
Fixed wing span	3.732 m
Wing airfoil	NACA 64A221
Number of blades	4
Rotor radius	3.7 m

Table 1: Reference full–scale aircraft details.

climbing flight whereas a cruise speed of $V_{cruise} = 170\ m/s$ was required in aeroplane mode. Due to the high cruise speed considered, the blade tip sections are characterised by high Mach numbers that are responsible for the onset of drag rise.

The aerodynamic shape design of the tiltwing tiltrotor blade was carried out with a two–level optimisation procedure, summarised in Figure 1. Although the reduction of radiated noise often represents one of the objectives in modern rotorcraft optimisation activities, it should be observed that the blade optimisation procedure here proposed is free from any kind of acoustic constraints. This choice was made because official certification criteria for tiltrotor aircraft are not available [14] and flight conditions generating maximum noise levels (as for example Blade–Vortex Interactions (BVI) in low speed descent flight [14] in helicopter mode) are different with respect to the flight conditions considered in the present study.

At a first level, a multi–variable multi–objective optimisation procedure was used in the frame of the

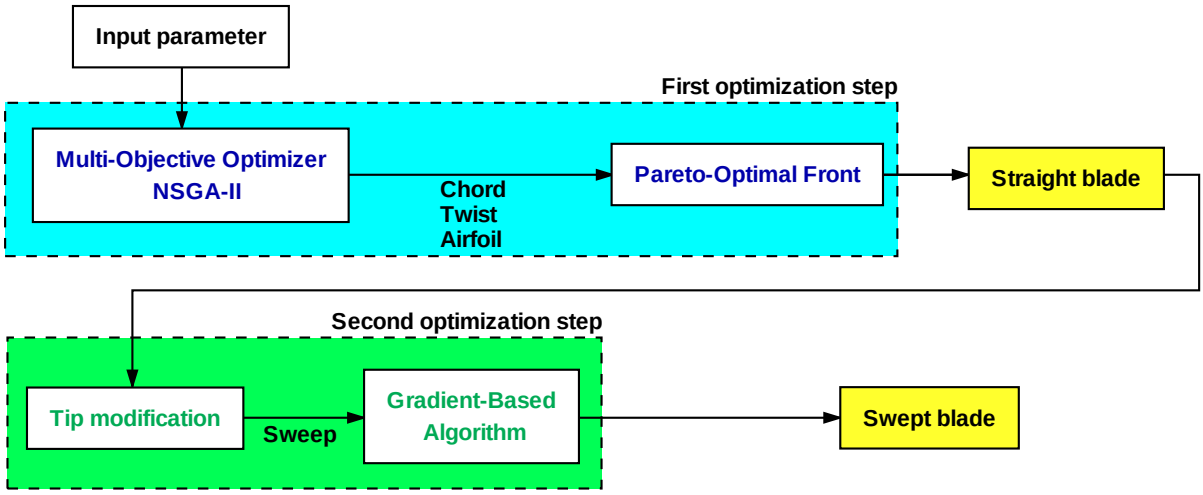

Figure 1: Sketch of the two–steps optimisation procedure.

genetic optimisation technique in order to obtain an optimal blade geometry in terms of twist, chord and airfoil distributions. As the classical BEMT approach was used to compute the rotor performance, the sweep angle effects were not predictable and therefore no sweep angle distribution was taken into account at this stage. The multi–objective optimiser tended to evolve individuals towards the Pareto–Optimal Front (that is a set of solutions that are non–dominated with respect to each other [23]). At the end of the first phase of the optimisation process, the resulting optimal blade was identified among the individuals included in the Pareto–Optimal Front as the blade which gave the best compromise in terms of performance between different objectives. However, once the Optimal–Pareto Front was found, the optimiser was not able to identify an optimal individual that could be considered better than the others, so the choice of the optimal blade could not be directly accomplished by the optimiser. Indeed, since Pareto Fronts in general and the Optimal–Pareto Front in particular were identified by performing the non–dominated sorting procedure over individuals of a given population [23], all the individuals belongings to the Optimal–Pareto Front represented optimal solutions with respect to the analysed objectives. The choice of the optimal blade could not be done automatically and was hence carried out after a careful examination of the Optimal–Pareto Front. In particular, different individuals were compared with one another in terms of rotor performance, loads and variable distributions. Each flight condition accounted for the optimisation was analysed with respect to several trim conditions in addition to the design one (i.e. different C_T/σ). Individuals showing poor performance in one or more flight conditions were rejected, as well as individuals exhibiting undesired load distributions in certain trim conditions (i.e. premature stall of a blade portion). An individual exhibiting good performance in all flight conditions was finally identified: it represented the best compromise solution

for the analysed problem among the individuals included in the Optimal–Pareto Front.

At the second level of the optimisation procedure, the selected optimal blade was then refined to reduce power losses due to the onset of compressibility effects near the blade tip in aeroplane flight mode. With the goal of improving the proprotor performance in this operative condition, the normal Mach number criterion was used to modify the tip shape introducing a non–linear sweptback angle Λ and moving the outer sections of the blade backward. Even thought this solution reduces tip power losses, the backward displacement of the outer blade sections resulted in an overall increase in the aerodynamic torsional moment M_t around the blade feathering axis, both in helicopter and in aeroplane flight mode. Therefore, in order to balance the blade aerodynamic torsional moment, a non–linear sweep angle distribution was introduced in the inner part of the blade moving ahead the corresponding sections. The displacement of the inner blade sections was calculated making use of a gradient–based algorithm which attempted to find a minimum of a scalar objective function of several variables under prescribed constraints. The algorithm used the values of the objective function as well as its gradient in order to find a new search direction, starting from an initial guess. The initial estimate solution array corresponded to the spatial displacement of the blade sections at the end of the tip refinement phase.

Note that the two–level optimisation procedure here described (see Figure 1) could be included in a closed loop and so repeated several times in order to better refine the blade shape in terms of variables distributions. In principle, this strategy could be adopted to include the optimal blade generated at the end of one complete iteration in the initial population of the successive multi–objective optimisation. However, since the multi–objective genetic optimiser managed only chord, twist and airfoil distributions because the BEMT solver was not able to predict the sweep angle effects, the information about the sweep distribution resulted unnecessary and would have been unused in the first optimisation level.

3.1 First–level optimisation

All of the flight conditions described above were taken into account in the first–level of the optimisation procedure. As a consequence, three different objectives were maximised simultaneously by the multi–objective optimisation algorithm. In the hovering flight, the objective was to maximise the rotor FM. In climb and in cruise conditions the objective was to maximise the propulsive efficiency, respectively η_{climb} and η_{cruise}. For a hovering rotor the FM is defined as the ratio between the ideal power required to hover and the actual power required, and can be calculated using the simple momentum theory

[37, 16], that is:

$$FM = \frac{\text{Ideal power required to hover}}{\text{Actual shaft power required}} = \frac{C_T^{3/2}}{\sqrt{2}C_P}. \tag{1}$$

On the other hand, the same definition adopted for conventional propellers can be used to determine the propulsive efficiency of a proprotor rotor [16]. It follows that the propulsive efficiency can be defined as the ratio between the ideal propulsive power and the actual power needed to produce the thrust, that is:

$$\eta = \frac{\text{Ideal propulsive power}}{\text{Actual shaft power required}} = \frac{TV_\infty}{P}, \tag{2}$$

where V_∞ represent the free stream velocity of the aircraft.

In the first level of the optimisation chain, the rotor blade shape geometry was described by means of three different parameters at given sections. The chord, the twist, and the airfoil shape index are chosen by the optimiser for each section, and the blade design variables array $\mathbf{x}$ was defined as follows:

$$\mathbf{x} = (\ldots, c_i, \ldots, \theta_i, \ldots, ASI_i, \ldots)^T. \tag{3}$$

Blade sections are supposed to be aligned along the blade feathering axis which passes through 25 % of the local chord. Note that in the first–level of the optimisation procedure, neither horizontal nor vertical relative displacements of the sections were taken into account. Each design variable law was parametrised by an interpolating cubic spline having 9 control points along the blade radius. This number was chosen in order to have three design sections in each part of the blade (inner, middle and outer), providing a more effective control on variable laws. On each section, a set of upper and lower bounds are prescribed on the design variables, so that a given feasible solution was found in the range between them. Chord and twist variable bounds were identified on the basis of preliminary calculations and were shown in Figure 2(a) and 2(b). In this regard, chord and twist distributions of existing tiltrotors [8, 9, 11, 14] and propeller driven aeroplane [49, 50] blades were used to identify plausible mean distributions along the blade span. Upper and lower bounds were hence defined as the sum of the resulting local mean value and the corresponding standard deviation multiplied by a coefficient initially equal 2. In order to avoid undesired variable distributions in the solution, such as variables convergence toward upper or lower bounds, preliminary single and multi–objective optimisations were performed to calibrate coefficients. The final set of chord upper and lower boundaries was obtained with a minimum coefficient of 4 (outer blade section) and a maximum coefficient of 6 (fifth section) while a minimum coefficient of 3.5 (outer three blade sections) and a maximum coefficient of 5 (fourth section) were found for the twist boundaries. The airfoil shape index bounds are reported in Figure 2(c) and were chosen so as to arrange suitable airfoils depending on the section position along the blade span. The available airfoil sections were ordered so that airfoils

with low indices were placed in the inner part of the blade, while airfoils with high indices were used toward the tip. As consequence, the optimiser was forced to use symmetrical airfoil sections (NACA four digits airfoils) in correspondence of the blade inner part, high–lift airfoils having high maximum lift coefficients and low pitching moments in the middle of the blade and thin airfoils designed for high–speed free stream conditions (high Mach numbers) at the blade tip.

Linear equality and inequality constraints were defined on the design variables and were supplied to the optimiser in order to guide the solution towards feasible blade geometries avoiding undesired solutions. In particular, chord and twist constraints were designed to obtain smooth transitions between successive sections in order to avoid manufacturing problems. Moreover, while chord constraints allowed to find a variable distribution with the maximum chord value located in the middle portion of the blade, twist constraints forced the resulting distribution to be monotonically diminishing. Since the optimisation requirements were given in terms of rotor thrust, in each operating condition the required thrust to fly represents a non–linear constraint which had to be reached by the rotor. As a consequence, every time the fitness function was computed, a trim problem was solved for each objective. Only when the trim condition was found the rotor performance were evaluated. In hover, the rotor thrust requirement was equal to half the aircraft weight ($T_r = 53464\ N$, see Droandi's doctoral dissertation [33] for details), while in vertical climb, the required thrust corresponded to the sum of the aircraft half weight with the airframe half drag ($T_r = 55072\ N$, see [33]). On the other hand, in cruise flight at high speed, the rotor thrust corresponded to half the aircraft drag ($T_r = 11288\ N$, see [33]).

3.2 Second–level optimisation

In order to reduce power losses in aeroplane mode, the optimal blade given by the multi–objective optimiser was further modified near the tip. The tip shape refinement problem was treated with a simple approach commonly employed in helicopter rotor design [17, 51, 22]. In this regard, by referring to the cruise flight condition, the normal Mach number criterion was used to calculate a progressive non–linear sweptback angle Λ needed to move the supersonic region towards the blade tip. The sweep angle Λ was computed to keep the incident Mach number M_n constant and below the sectional drag divergence Mach number M_{dd}. According to the BEMT approach [18], the local sweep angle Λ can be written as follows:

$$\Lambda = \cos^{-1}\frac{M_n}{M} = \cos^{-1}\frac{M_{dd}c_\infty}{\sqrt{U_T^2 + U_P^2}}. \tag{4}$$

Equation 4 was computed for all sections near the blade tip where the local M_n was higher than the M_{dd} associated with the given airfoil section. The corresponding airfoil sections were moved

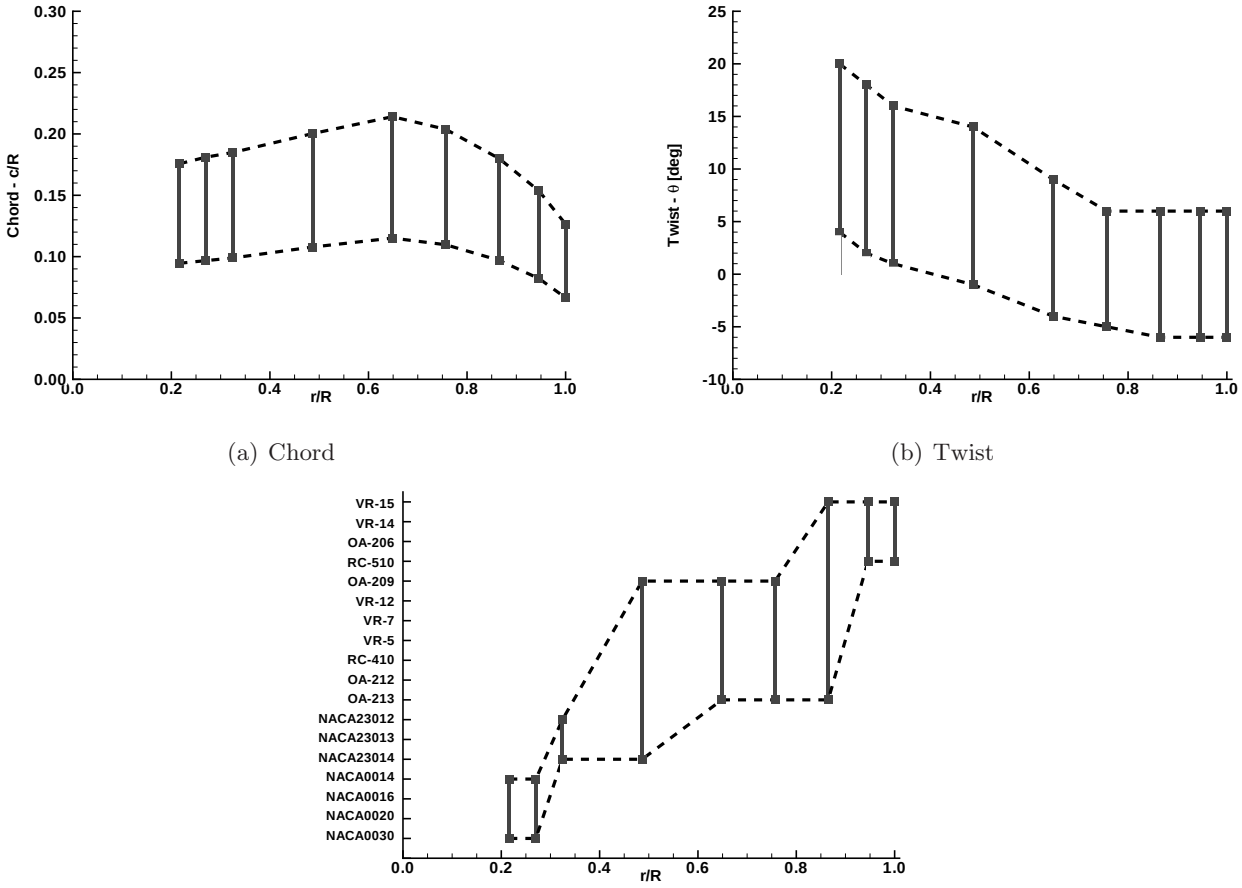

(a) Chord

(b) Twist

(c) Airfoil shape index

Figure 2: Design variable limits and span–wise location of design sections.

backwards by applying the sweep angle with reference to the blade feathering axis. It follows that, at the end of this process, the aerodynamic centres of the outer blade sections were located behind the blade feathering axis. In order to limit the aerodynamic torsional moment around the pitch hinge for widest possible range of pitch angle, the hinge is commonly located in correspondence of the blade aerodynamic centre, thus in the present case the aerodynamic torsional moment on the blade is balanced at the hinge by moving the inner blade sections forward. A non–linear law describing the sweep angle distribution in the inner part of the blade was hence computed by requiring that the resulting blade aerodynamic torsional moment was independent from the trim pitch angle θ_0. The blade pitch angle θ_0 was defined as the angle between the plane normal to the rotor axis and the blade root section, so that for a null θ_0 the first blade section had a geometrical incidence of 9.061°. This request represented the objective of the single–variable optimisation carried out by means of the gradient–based optimiser. The optimisation variable was represented by the local sweep angle Λ that was referred to the blade feathering axis. The resulting variable law was parameterized by an

interpolating cubic spline over a total number of 4 points uniformly distributed between the 40 % of blade radius and the first inner section in which the local M_n was higher than the sectional M_{dd}. The objective function was defined as the standard deviation of the aerodynamic torsional moments $M_{t,i}$ given by the blade in several trim conditions and can be written as follows:

$$\sigma_M = \sqrt{\frac{1}{N}\sum_{i=1}^{N}\left(M_{t,i} - \overline{M_t}\right)^2}. \tag{5}$$

In Equation 5, the aerodynamic moment $M_{t,i}$ has to be intended as the rotor global aerodynamic torsional moment evaluated by integrating the different blade element contributions, while $\overline{M_t}$ represents the mean value of all computed aerodynamic torsional moments. The optimiser attempted to minimise the objective function under linear inequality constraints. The local sweep angle value was also subject to lower and upper boundaries that were prescribed together with linear inequality constraints to avoid strong variation on section displacements that may lead to manufacturing problems.

4 Optimisation results and discussion

4.1 Multi–objective optimisation results

In the first–level of the optimisation procedure, the multi–objective genetic optimiser was run on a population of 70 individuals. The population size was carefully chosen in order to achieve a good compromise between genetic variability and computational time. Starting from a well–distributed initial population, the optimiser analysed 400 subsequent generations and the resulting Pareto–Optimal Front was composed of 25 optimal individuals. The results of the multi–objective optimisation procedure are reported in Figure 3 where the Pareto–Optimal Front obtained after 400 generations is compared with all individuals included in both the initial and final populations. As it can be observed, individuals belonging to the initial population were highly scattered in the feasible solution space and most of them exhibited poor performance both in helicopter and in aeroplane operative modes. On the other hand, individuals included in the final population were clearly flattened towards the Pareto–Optimal Front. Figure 4 illustrates the span-wise distribution of chord, twist and airfoil index of all 25 individuals belonging to the Pareto–Optimal Front. In order to select an optimal solution within the individuals that were part of the Pareto–Optimal Front, the performance and the geometrical characteristics of resulting blades were analysed in detail. The optimal blade was hence identified as the individual showing the best compromise between helicopter and aeroplane performance and having distributions of chord, twist and airfoil suitable for manufacturing. A summary of the selected blade geometrical characteristics is reported in Table 2. The span–wise distribution of chord, twist and airfoil index

shape is highlighted in black in Figure 4.

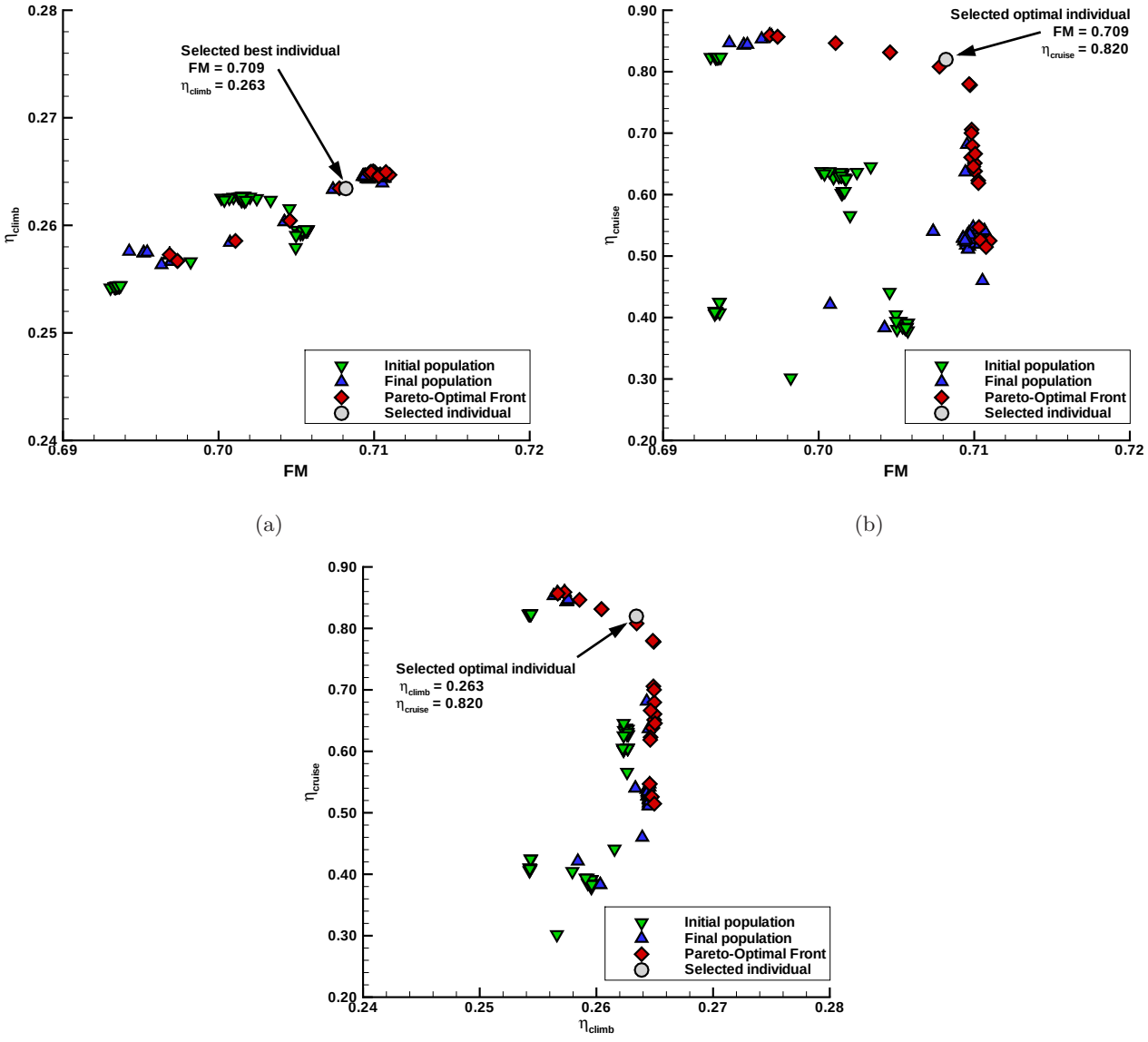

Figure 3: Results of the multi–objective optimisation procedure in the feasible solution space.

Figure 5 shows the performance of the selected optimal blade compared with the solutions maximising each single objective performance extracted from the Pareto–Optimal Front. For sake of completeness, the geometrical characteristics of the latter solutions are reported in Table 3. Indeed,

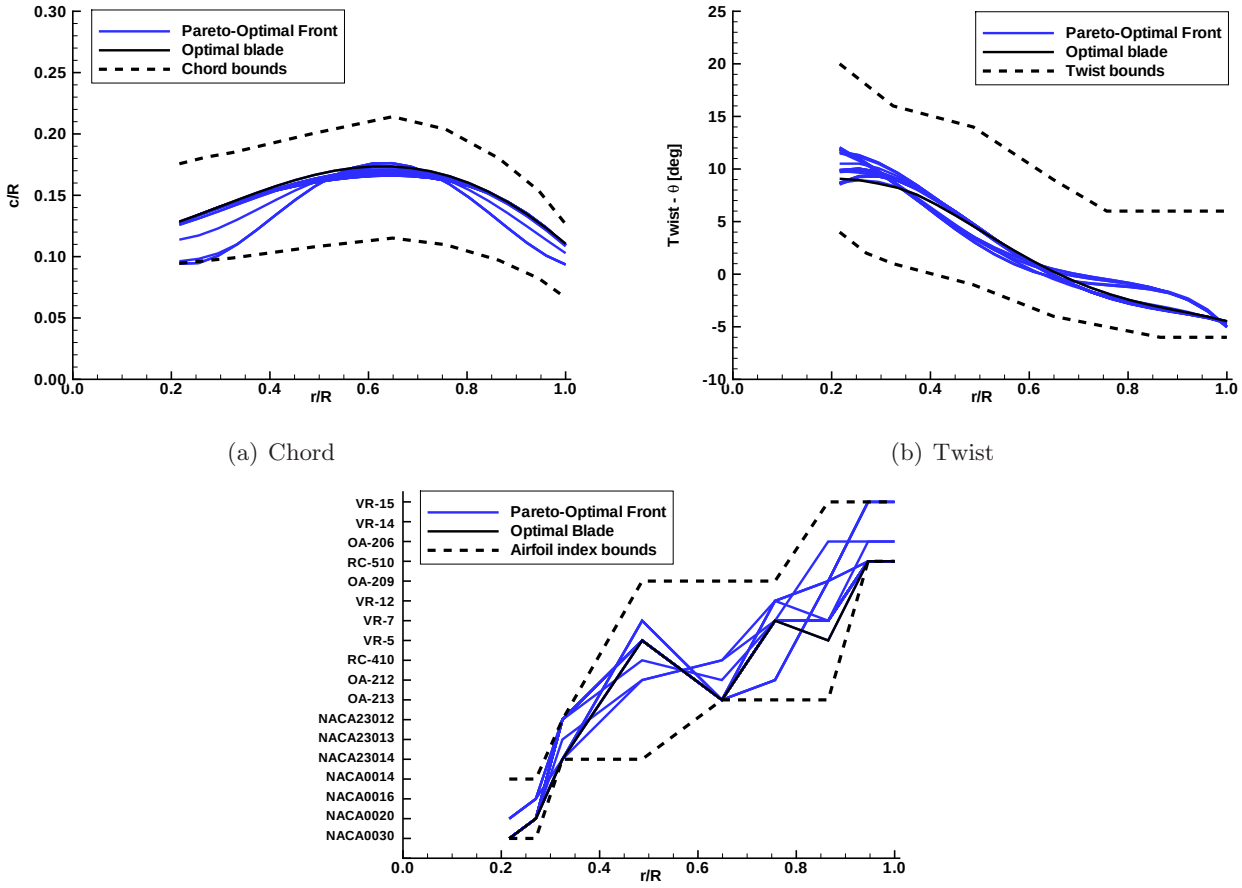

(a) Chord

(b) Twist

(c) Airfoil shape index

Figure 4: Span–wise chord, twist and airfoil distribution for individuals of the Pareto–Optimal Front.

Section	r/R	c/R	θ [deg]	Airfoil	$\Delta\zeta/R$	Λ [deg]
1	0.216	0.131	9.061	NACA 0030	0.000	0.0
2	0.270	0.133	8.351	NACA 0020	0.000	0.0
3	0.324	0.144	8.324	NACA 23014	0.000	0.0
4	0.487	0.168	5.217	VR–5	0.003	−4.2
5	0.649	0.179	−0.005	OA–213	0.017	−4.4
6	0.757	0.155	−2.265	VR–7	0.025	−4.7
7	0.865	0.154	−2.849	VR–5	−0.003	23.9
8	0.946	0.131	−3.540	RC–510	−0.046	26.0
9	1.000	0.108	−4.759	RC–510	−0.077	27.3

Table 2: Geometric characteristics of the optimised blade.

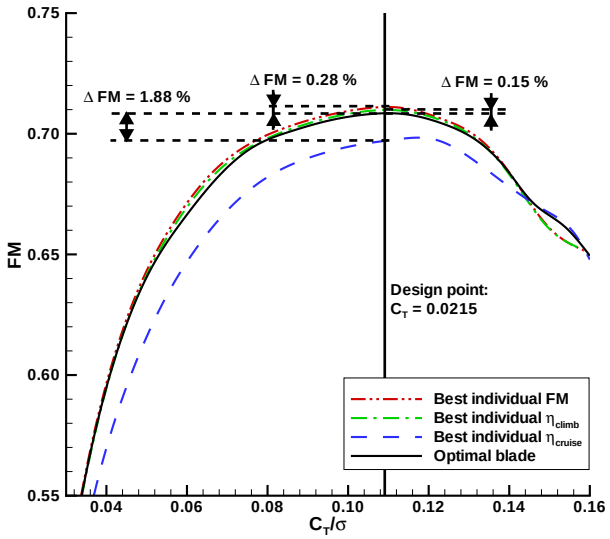

(a) Hover

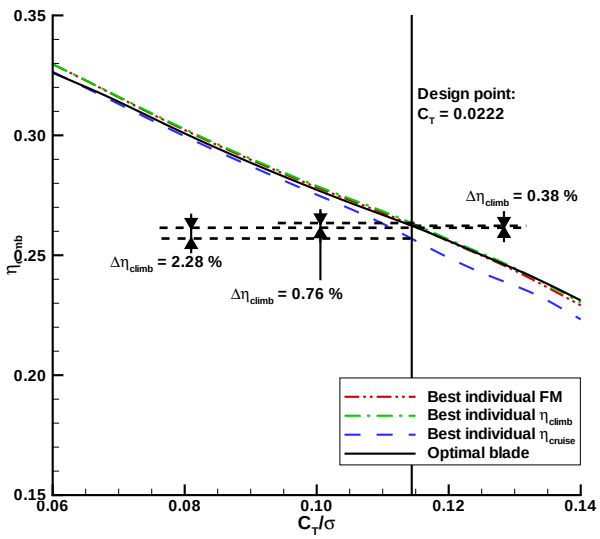

(b) Climb

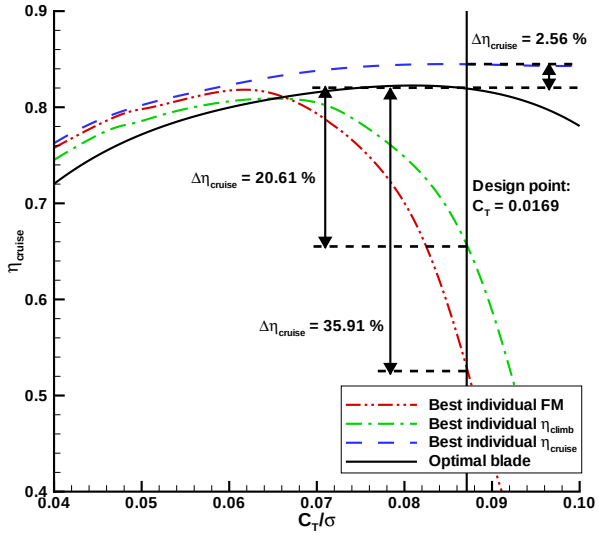

(c) Cruise

Figure 5: Performance analysis between individuals included in the Pareto–Optimal Front: comparison between optimal individual and individuals maximizing each objective.

the selected optimal solution presented, during hovering, a FM quite close to the maximum value achieved, and the difference at the design point was of the order of 0.3 %. Essentially the same result was found for the climbing flight, where the η_{climb} of the chosen individual was 0.38 % less than the maximum value obtained. In cruise flight the propulsive efficiency of the selected blade was 2.56 % less with respect to the best solution for the cruise condition. It is important to observe that the optimal blade extracted from the Pareto–Optimal Front represented the individual that exhibited good performance in all the analysed flight conditions. Indeed, the other individuals, and in particular

	Best FM			**Best η_{climb}**			**Best η_{cruise}**		
Section	c/R	θ [deg]	Airfoil	c/R	θ [deg]	Airfoil	c/R	θ [deg]	Airfoil
1	0.128	11.652	NACA 0030	0.128	9.805	NACA 0030	0.096	12.027	NACA 0030
2	0.136	11.027	NACA 0020	0.136	9.543	NACA 0020	0.099	10.445	NACA 0020
3	0.144	9.869	NACA 23012	0.144	9.059	NACA 23014	0.108	8.715	NACA 23014
4	0.161	4.573	RC–410	0.162	4.750	VR–5	0.156	3.563	VR–7
5	0.166	−0.189	OA–212	0.168	−0.122	OA–213	0.176	0.488	OA–213
6	0.162	−2.171	VR–7	0.163	−2.228	VR–7	0.160	−0.490	OA–212
7	0.148	−3.277	VR–7	0.148	−3.361	VR–5	0.130	−1.512	OA–209
8	0.128	−3.942	RC–510	0.127	−4.024	RC–510	0.105	−3.152	VR–15
9	0.111	−4.497	RC–510	0.110	−4.607	RC–510	0.094	−4.935	VR–15

Table 3: Geometric characteristics of individuals maximising each objective and included in the Pareto–Optimal Front.

the individuals maximising each single objective, exhibited worse performance than the selected blade when the other flight conditions were taken into account. The best individual for the cruise condition presented a reduction of 1.88 % in terms of FM with respect to the selected blade at the design point in hover. Similarly, the best individuals for the hovering and climbing flight showed a reduction of η_{cruise} respectively of 35.91 % and 20.61 % when compared to the optimal individual at the design point in cruise flight. In conclusion, the selected blade was considered as the best compromise solution because the hovering and climbing conditions were the most demanding in terms of required power and fuel consumption since the aircraft mission requirements included significant hover and near–hover duration. The values of the pitch trim angle, required power coefficient and rotor efficiency of the aforementioned blade solutions at the three design conditions accounted are listed in Table 4. A summary of hover, climb and cruise efficiency increases found comparing the optimal selected blade with individuals maximising each single objective (extracted from the Pareto–Optimal Front) are shown in Figure 6(a). Even though many individuals included in the Pareto–Optimal Front gave low performance at least in one flight condition, they exhibited better performance with respect to individuals included in the initial population. In order to assess the improvements given by the multi–objective optimisation process, the performance of the optimal selected blade in hover, climb and cruise conditions was compared with the results of single objective optimisations carried out at the beginning to build the initial population. In Figure 6(b) this comparison is presented for each flight condition taking into account the efficiency increases obtained for the selected blade with respect to

best individuals resulting from single objective optimisations. As it can be observed, for a given flight condition, the optimal blade showed a performance (i.e. FM, η_{climb} or η_{cruise}) that was very similar (less than 0.5 %) to the performance given by the individual coming from the corresponding single objective optimisation. On the other hand, when the optimal blade was compared with individuals optimised for different flight conditions, the efficiency increase was found to be substantially higher. In those cases, the efficiency increases also resulted to be higher than the increases measured in the cases of individuals extracted from the Pareto–Optimal Front.

Hovering flight (Helicopter mode, $C_T = 0.0215$)			
Individual	θ_0 [deg]	C_P	FM
Best FM	13.9	0.00314	0.711
Best η_{climb}	13.9	0.00315	0.710
Best η_{cruise}	15.2	0.00321	0.696
Selected blade	13.7	0.00316	0.709
Climbing flight (Helicopter mode, $C_T = 0.0222$)			
Individual	θ_0 [deg]	C_P	η_{climb}
Best FM	16.1	0.00384	0.264
Best η_{climb}	16.1	0.00382	0.265
Best η_{cruise}	17.5	0.00396	0.257
Selected blade	15.9	0.00388	0.263
Cruise flight (aeroplane mode, $C_T = 0.0169$)			
Individual	θ_0 [deg]	C_P	η_{cruise}
Best FM	66.6	0.0324	0.525
Best η_{climb}	64.7	0.0294	0.651
Best η_{cruise}	57.5	0.0204	0.841
Selected blade	58.3	0.0210	0.820

Table 4: Performance (pitch trim angle, power coefficient and rotor efficiency) in helicopter and aircraft configurations: comparison between optimal individual selected from the Pareto–Optimal Front and individuals maximising each objective included in the Pareto–Optimal Front.

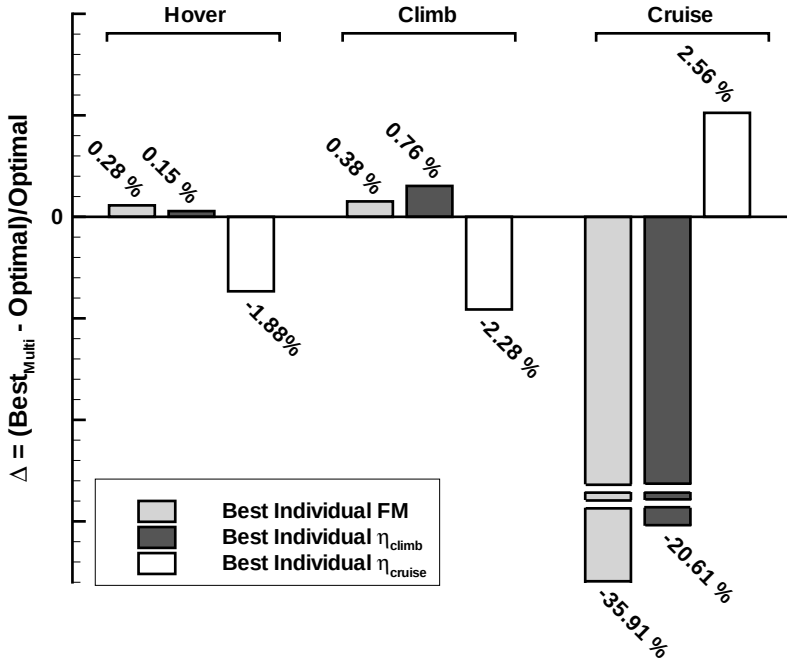

(a) Performance increase (percent) between optimal blade and individuals maximising each objective included in the Pareto–Optimal Front

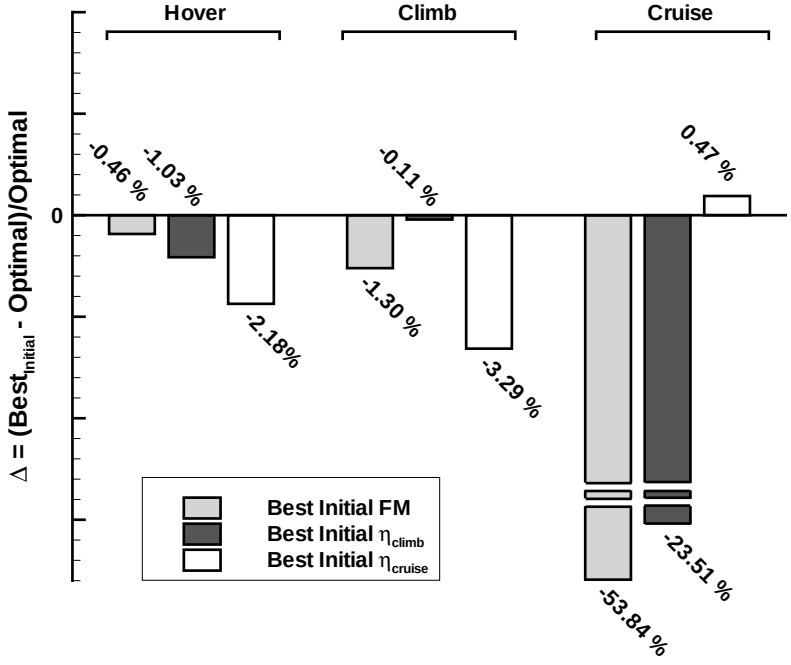

(b) Performance increase (percent) between optimal blade and best individuals resulting from single objective optimisations (included in the initial population)

Figure 6: Increase in hover, climb and cruise efficiency.

4.2 Tip refinement

In the second–level of the optimisation procedure, the optimal blade extracted from the Pareto–Optimal Front at the end of the previous phase was refined by trying to delay the onset of drag rise and consequently of compressibility losses. For this purpose, the blade tip was modified designing a non–linear sweep angle distribution to move the outer sections of the blade backward. The analysis was carried out taking into account the same sections considered in the previous optimisation phase without changing other blade characteristics, such as sectional twist and chord. The resulting blade, modified at the tip, is reported in Figure 7, where it is compared with the selected optimal blade (unswept) coming from the Pareto–Optimal Front. In the figure, the modified blade is superimposed on the original unswept blade in order to highlight the shape modification at the blade tip.

As previously explained, a second optimisation step was performed on the modified blade. In particular, in order to prevent structural and stability problems on the rotor, some sections in the middle part of the blade were moved ahead. A non–linear sweep angle distribution in this region of the blade was found making use of a gradient–based optimiser which attended to balance the aerodynamic

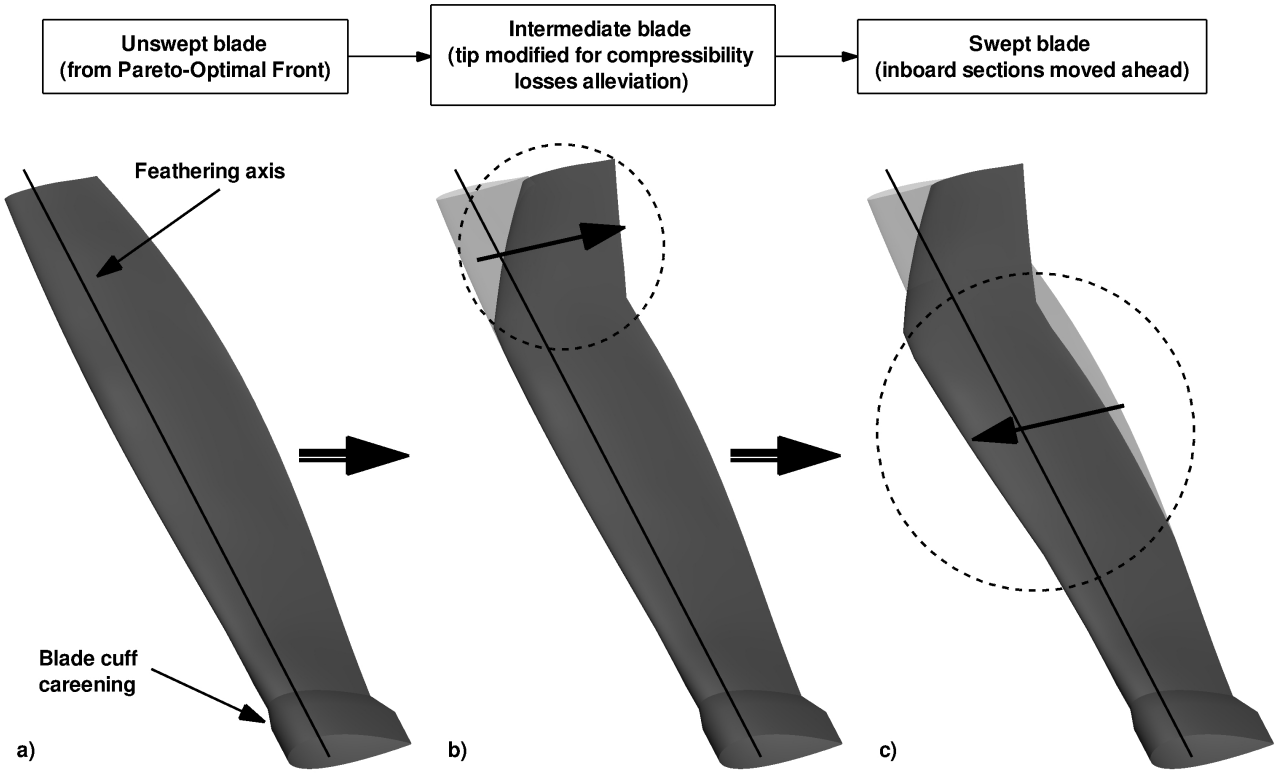

Figure 7: Comparison between a) the original blade (unswept), b) the blade with modified tip for delay of compressibility losses (intermediate) and c) final blade with inboard section displacement (swept).

torsional moment on the blade axis, making it independent from the trim pitch angle θ_0. The outer sections of the blade, previously modified by following the normal Mach number criterion, were once more modified to adapt them to the new inboard sweep angle distribution. The final shape of the blade is illustrated in Figure 7 where it is directly compared with the original unswept blade. The non–linear sweep angle distribution is reported in Table 2 together with other blade geometrical characteristics. The resulting local displacement of the blade sections ζ/R and the sweep angle distribution are also shown in Figure 8.

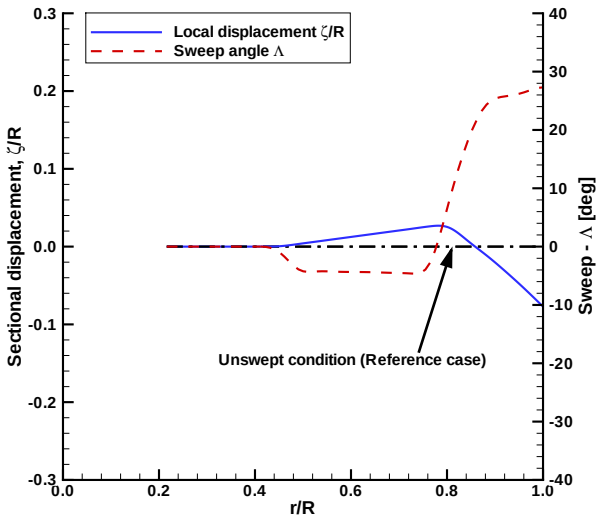

Figure 8: Span–wise sectional displacement ζ/R and sweep angle Λ distribution.

5 Validation of results

5.1 CFD analysis

In order to obtain more accurate evaluations of the optimised blade performance, numerical calculations were carried out with the CFD code ROSITA. In particular, CFD computations were used to verify both the BEMT solver predictions and the effects caused by the introduction of the sweep angle distribution along the blade. The axisymmetrical flow conditions considered (hovering and axial flight) and the circumferential periodicity of the rotor wake geometry allowed to introduce some useful simplifications for CFD calculations. Indeed, numerical simulations were carried out only on a 90° cylindrical sector around a single blade with periodic boundary conditions on the sides. It follows that the control volume that would contain the whole rotor can be reduced to one fourth. The computational mesh was composed of 2 different structured multi–block grids. The first one represented the background flow region in which the blade was located, Figure 9(a), and the second one the blade

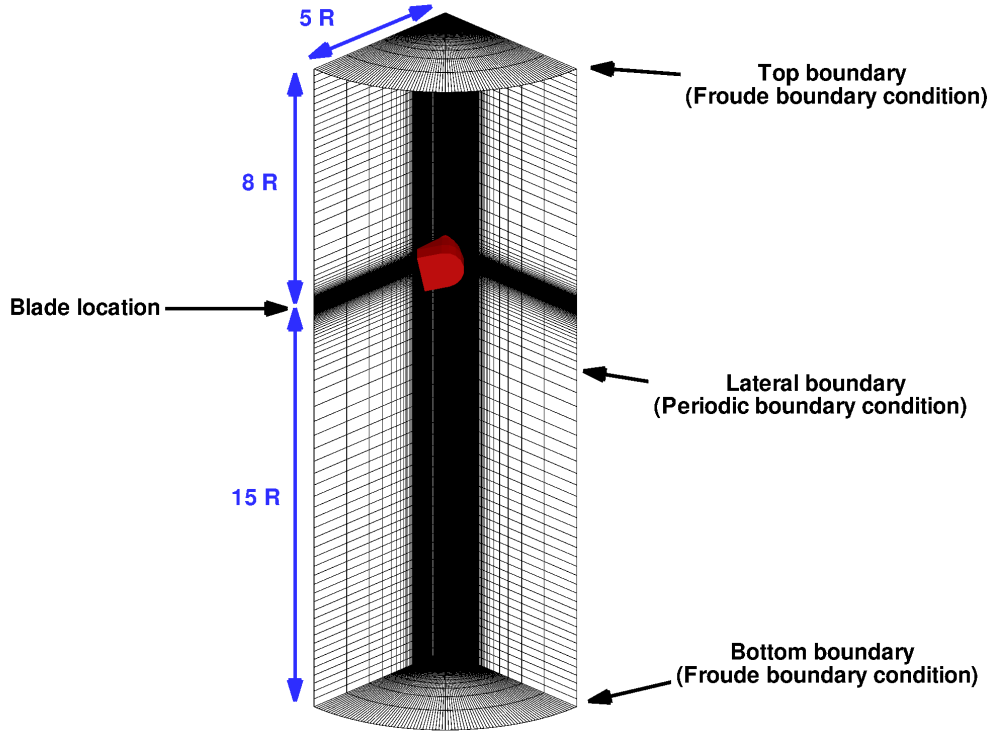

(a) View of the grid system

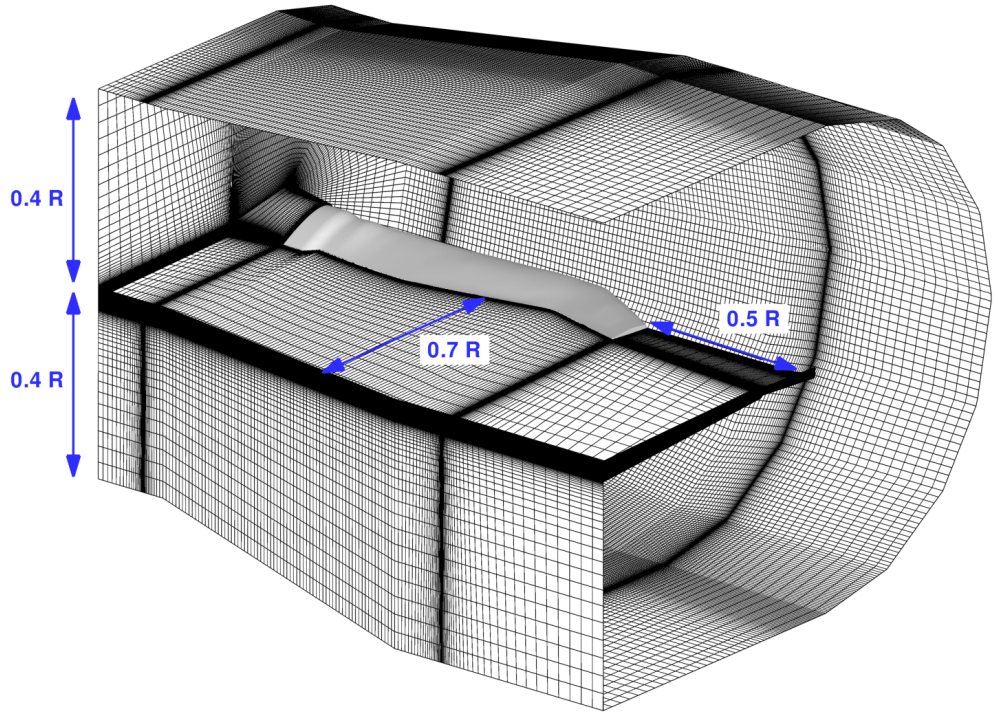

(b) Blade grid details

Figure 9: CFD grid details.

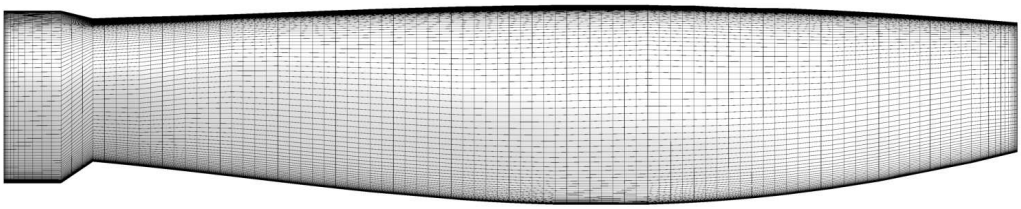

(a) Unswept blade

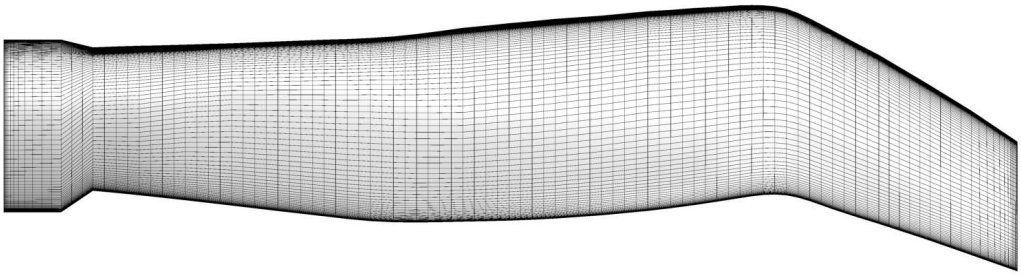

(b) Swept blade

Figure 10: Surface grid.

and the flow region close to it, Figure 9(b). The background grid had an O–H monoblock meshing topology containing a total of about 1.2×10^6 cells with the outer boundaries located 4 R from the blade tip in the span–wise direction, 8 R above and 15 R below the rotor plane in vertical direction. Since the ROSITA Navier–Stokes solver was used to verify optimisation results, two similar grids were built in order to represent both the swept and unswept blade geometries. A C–O grid multiblock meshing topology was used to limit the global grid size and to ensure a very good nodes distribution and orthogonality in the proximity of the blade surface. In both cases, the first layer of elements near the blade surface had a height of 4×10^{-6} R which corresponds to the value of the dimensionless wall distance ($y+ = 1$). This value was based on the flow conditions (i.e. the Reynolds and Mach number) at the blade tip. The blades were discretised using a hyperbolic law along the chord–wise, span–wise and normal surface directions having similar spatial resolution. The surface grid of both analysed blades are reported in Figure 10. Note that both swept and unswept blades had straight root and tip. The outer boundaries were located at 0.4 R from the blade surface except in the span–wise direction, where they were at 0.5 R from the tip, and in the trailing edge region where they were at 0.7 R. The blade grids contains a total of about 3.2×10^6 cells distributed in 8 blocks. Efficient computations for hovering flight condition can be carried out by imposing the farfield Froude boundary conditions [52] on the top and bottom sections of the background grid, while classical periodic boundary conditions are

set on the two periodic faces on the background grid sides. A no–slip boundary condition was applied on the blade surfaces. All the aforementioned grids were created making use of ANSYS ICEMCFD.

Simulations were carried out both for the hovering flight condition in helicopter mode and for the cruise flight condition in aeroplane mode. The blade tip Mach number M_{Tip} was fixed at 0.64 for the hovering flight and at 0.54 for the cruise flight. Since the rotor rotational speed was fixed, in order to change the rotor thrust, only a collective pitch command was given to the blades. Also the Reynolds number based on the rotor radius and on the rotor tip speed was fixed during calculations and was equal to 5.5×10^7 in the hover case and to 2.2×10^7 in the cruise flight condition.

Figure 11 shows the comparison between the swept and unswept blades performance as function of C_T/σ both in hover and in cruise flight conditions. In this figure, CFD results are also compared with the BEMT prediction for the unswept blade. As expected, the integration of the sweep angle distribution along the span of the blade gave considerable performance improvements with respect to the unswept case. In hover, the rotor FM increased by around 1.5–2 % for C_T/σ higher than 0.06 reaching a value of 0.72 at the design point. In cruise flight, the rotor η_{cruise} was about 1.5 % higher than the unswept blade efficiency having a value of 0.83 at the design point. As it can be observed, in both flight conditions a rather good agreement is noticeable when comparing the simple strip theory results with CFD calculations carried out for the unswept blade. Under such comparison, the difference between the BEMT and CFD predictions at the design points in terms of FM and η_{cruise} are less than 0.2 %.

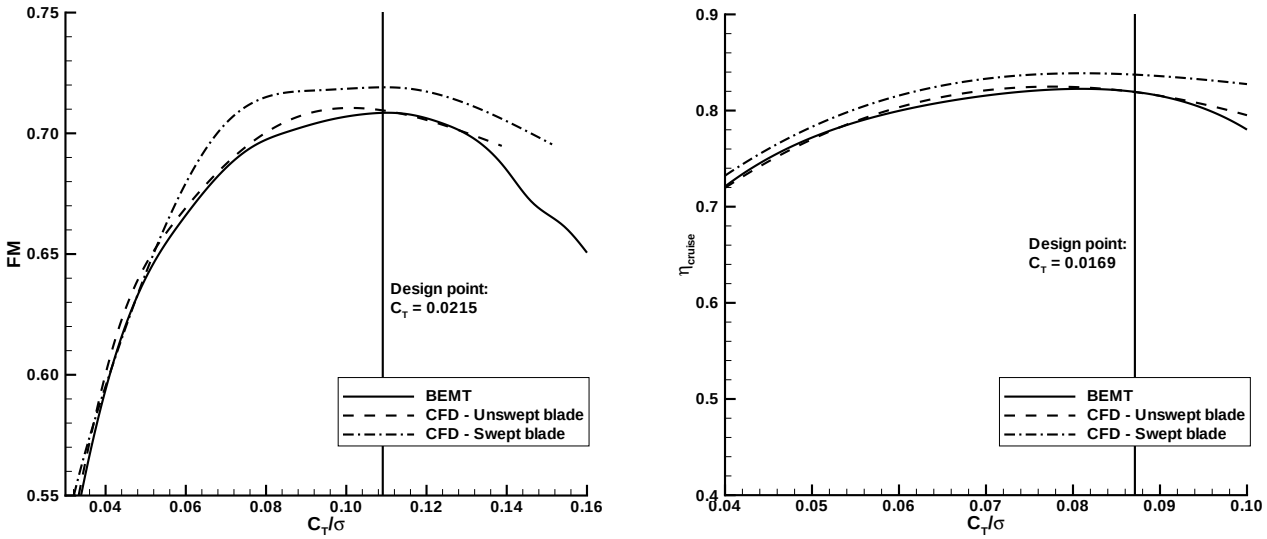

(a) Hover

(b) Cruise

Figure 11: Effect of the sweep angle on the blade performance: comparison between BEMT prediction and CFD calculations.

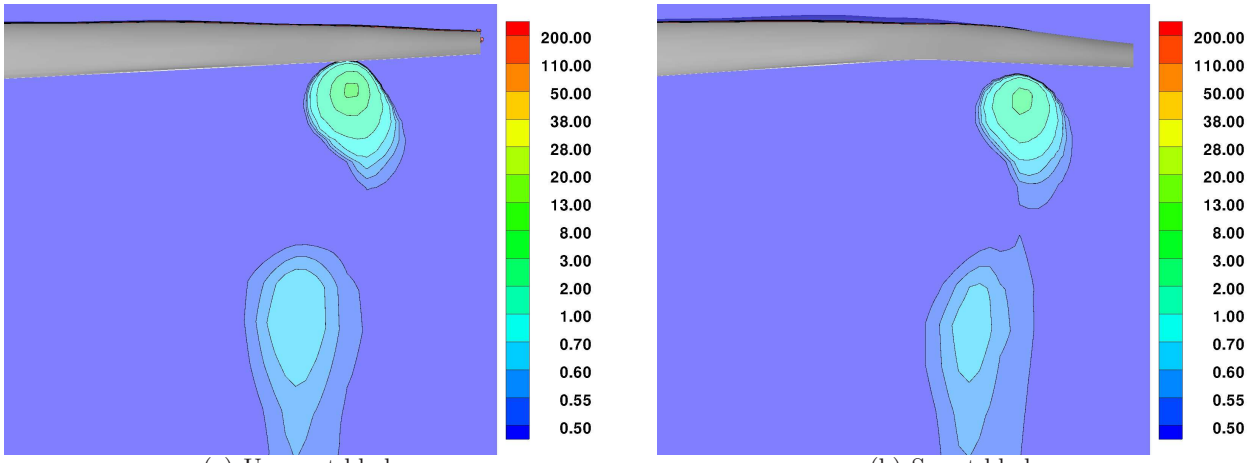

(a) Unswept blade (b) Swept blade

Figure 12: Unswept ($C_T = 0.0217$) and swept ($C_T = 0.0213$) blade in hovering at $\theta_0 = 14°$ and $M_{Tip} = 0.64$. Comparison between Q–criterion contours in a radial planes at $\psi = 0°$.

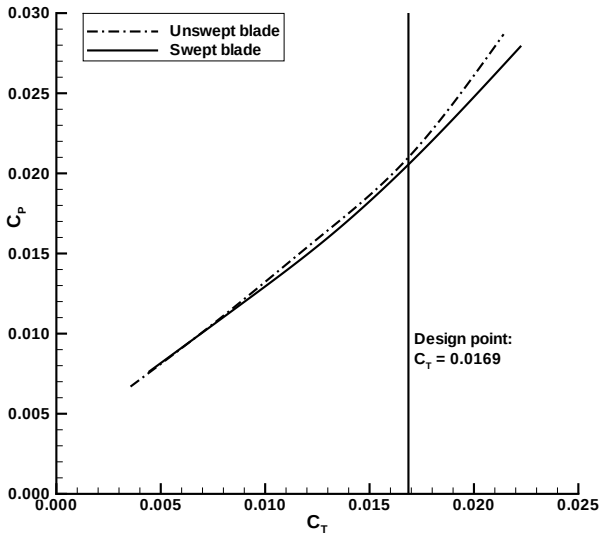

Figure 13: C_P as function of C_T in cruise: comparison between unswept and swept blade in cruise at $M_{Tip} = 0.54$, $M_\infty = 0.55$.

The difference between the hover performance of the swept and unswept blades can be mainly justified by the presence of a sort of anhedral effect [37], [19] in the swept case. In this case, the anhedral effect is mainly due to the combination of the effects given by the sweep angle Λ, distributed along the blade span, and the collective pitch angle θ_0, used to trim the rotor. Indeed, the non–linear sweep angle distribution slightly modifies the position of the blade tip vortex emission with respect to the unswept blade. The blade tip vortex is hence moved below the rotor plane and it is convected downstream, far from the lower surface of the blade. As a consequence, in the swept case the anhedral

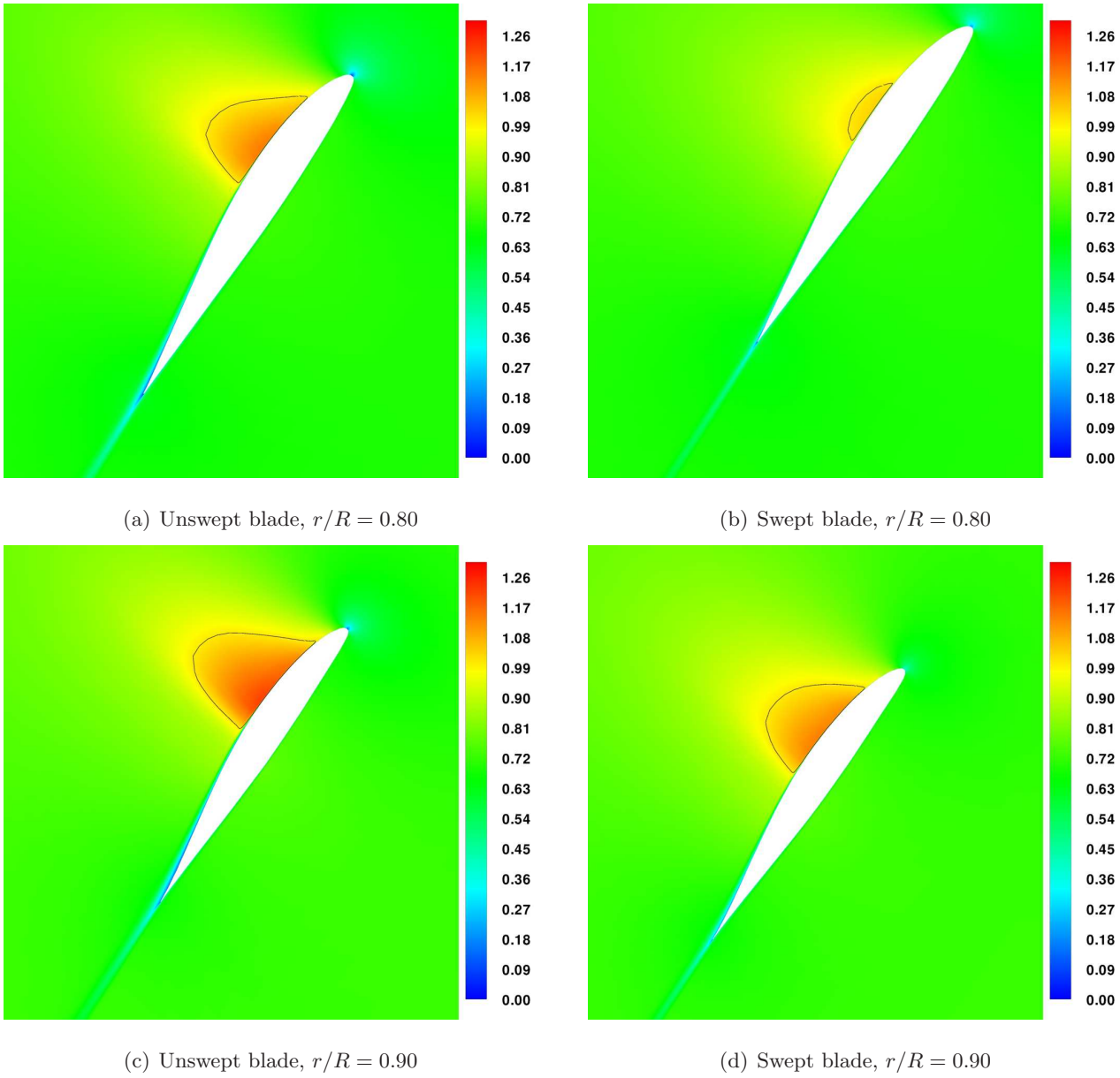

(a) Unswept blade, $r/R = 0.80$

(b) Swept blade, $r/R = 0.80$

(c) Unswept blade, $r/R = 0.90$

(d) Swept blade, $r/R = 0.90$

Figure 14: Unswept and swept blade in cruise flight at $C_T = 0.0169$, $M_{Tip} = 0.54$ and $M_\infty = 0.55$: sectional Mach contours and sonic line (in black).

effect significantly reduces the interaction between a given tip vortex and the following blade, so it increase the rotor performance in hover. In Figure 12 the flow fields around both the swept and unswept blades ($\theta_0 = 14°$) are illustrated by means of the contours of the Q–criterion for an azimuthal blade position equal to $\psi = 0°$. The influence of this sort of anhedral effect can be clearly observed in Figure 12 by looking at the positions of the tip vortices with respect to the corresponding blade.

In aeroplane flight mode, the comparison between the swept and unswept blade shows a general increase of the swept blade performance and highlights a substantial decay of the unswept blade

η_{cruise} after the design point, as reported in Figure 11(b). Indeed, in order to reach the same C_T, as illustrated in Figure 13, the unswept blade required more power with respect to the swept blade because it is characterised by higher power losses due to the onset of compressibility effects near the blade tip. In this regard, the positive effect of the backward displacement of the outer blade sections is proved comparing the flow field close to the tip of both blades. Figure 14 shows the comparison at the design cruise C_T between the Mach number contours around two sections near the blade tips ($r/R = 0.8$ and 0.9). As indicated by the black line, representing the sonic line, the supersonic region is significantly reduced in the swept case confirming that the sweep angle distribution allows to delay the onset of compressibility effects on the outer sections of the blade and limits the power losses in this region. Furthermore, the sweep angle distribution gives much more benefits for C_T higher than the design C_T in cruise, as shown in Figure 13.

Finally, it can be observed that the pitch trim angle θ_0 computed by the BEMT solver in hovering ($\theta_0 = 13.7°$) and cruise ($\theta_0 = 58.3°$) flight conditions are almost equal to the ones predicted by the CFD analysis (equal to 13.8° in hover and 58.2° in cruise). Note that the rotor trim procedure employed in CFD analyses is the same procedure used by the BEMT solver (for further details, refer to Droandi's doctoral dissertation [33]). At the same time, the trim conditions predicted for the swept blade by means of CFD calculations are slightly different with respect to the unswept one. Indeed, the pitch trim angle for the swept blade is equal to 14.2° in hovering and to 58.0° in cruise flight. In hovering, the remarkable difference in predicting the pitch trim angle (2.8 %) is due to the anhedral effect that implies a different evolution of the blade tip vortex in the flow field below the rotor plane.

5.2 Experimental validation

An experimental model [33, 53] of the optimised proprotor was realised at the DAER Aerodynamics Laboratory of Politecnico di Milano. Since the geometrical scale of the model was 1/4 with respect to the full–scale aircraft, the rotor radius of the model was 0.925 m. The rotor blade model had straight root and tip, like the previously described CFD blade models. In Figure 15 the experimental test rig for the isolated rotor tests is shown inside the open test section of the Large Wind Tunnel of Politecnico di Milano. The rotor rotating in anti–clockwise direction, was powered by a hydraulic motor (maximum power 16 kW at 3000 rpm) located inside an aluminium basement. The rotor hub was placed at a height of 5 R from the ground and it was mounted on a rigid pylon that was located over the hydraulic motor. The rotor hub was fully articulated representing a typical helicopter rotor hub. Note that, even thought tiltrotor aircraft generally employed gimballed rotor hub to prevent dynamic instabilities in cruise flight at high–speed (whirl flutter [2]), the test rig available at the Large Wind Tunnel of

Politecnico di Milano and used in this work was characterised by classical helicopter rotor hub design. However, since the wind tunnel model was used only to investigate the hovering condition, the rotor aerodynamics could be considered independent from the rotor hub design. Therefore the difference between a fully articulated and gimballed rotor head was considered negligible. The thrust given by the rotor was measured by a six–component strain gauge hollow balance located under the rotor hub, while the torque was measured by a shaft instrumented with strain gauges. The instrumented shaft was joined to the transmission shaft by means of a torsionally stiff steel laminae coupling. The collective, longitudinal and lateral pitch controls were provided to the blades by means of three independent electric actuators acting on the rotor swashplate. On each electric actuator, a linear potentiometer was installed to have a feedback signal on the actual position of each command. Each blade was attached to the rotor hub through the flap, lead–lag and pitch hinges located in different positions. In particular, the lead–lag hinge was located beyond the flap hinge while the feathering bearing was placed further outboard. No dampers were fitted on the lead–lag hinge of the rotor model. To directly measure the pitch, lead–lag and flap angles on the rotor hinges, Hall effect sensors were employed on each blade hinge.

During the experimental tests, the nominal rotational speed of the rotor was $n = 1120\ rpm$. The tip Mach number was $M_{Tip} = 0.32$, which corresponds to 1/2 the tip Mach number of full–scale aircraft in helicopter mode. However, the maximum C_T measured during the experiments was slightly lower than the design one because of power limitations due to motor capacity.

The experimental tests were conducted on the isolated rotor to characterise the rotor performance in hover at different trim conditions. The experimental measurements were used to validate the numerical calculations carried out with the CFD code ROSITA. For this reason, further numerical simulations were performed on the same tests conditions of the experiments. The computational grids used for calculations were the same previously employed to evaluate the rotor performance (swept blade) after the blade tip refinement process. The isolated rotor performance in hover is shown in terms of FM, C_T/σ and C_P/σ in Figure 16. The maximum value of FM measured during the experiments was 0.71 at $C_T/\sigma = 0.092$ and $C_P/\sigma = 0.012$. In Figure 16, the computed rotor performance both in experimental test conditions ($M_{Tip} = 0.32$) and at full–scale ($M_{Tip} = 0.64$) is also presented. As it can be observed, the agreement between experimental data and numerical results is very good.

For the hovering rotor, the comparison between the experimental data acquired during the tests and numerical results verifies the capability of the Navier–Stokes solver to predict the rotor performance in different trim conditions. Moreover, the comparison demonstrates that the ROSITA code is able to correctly predict the global loads acting on the hovering rotor. The impressive agreement between

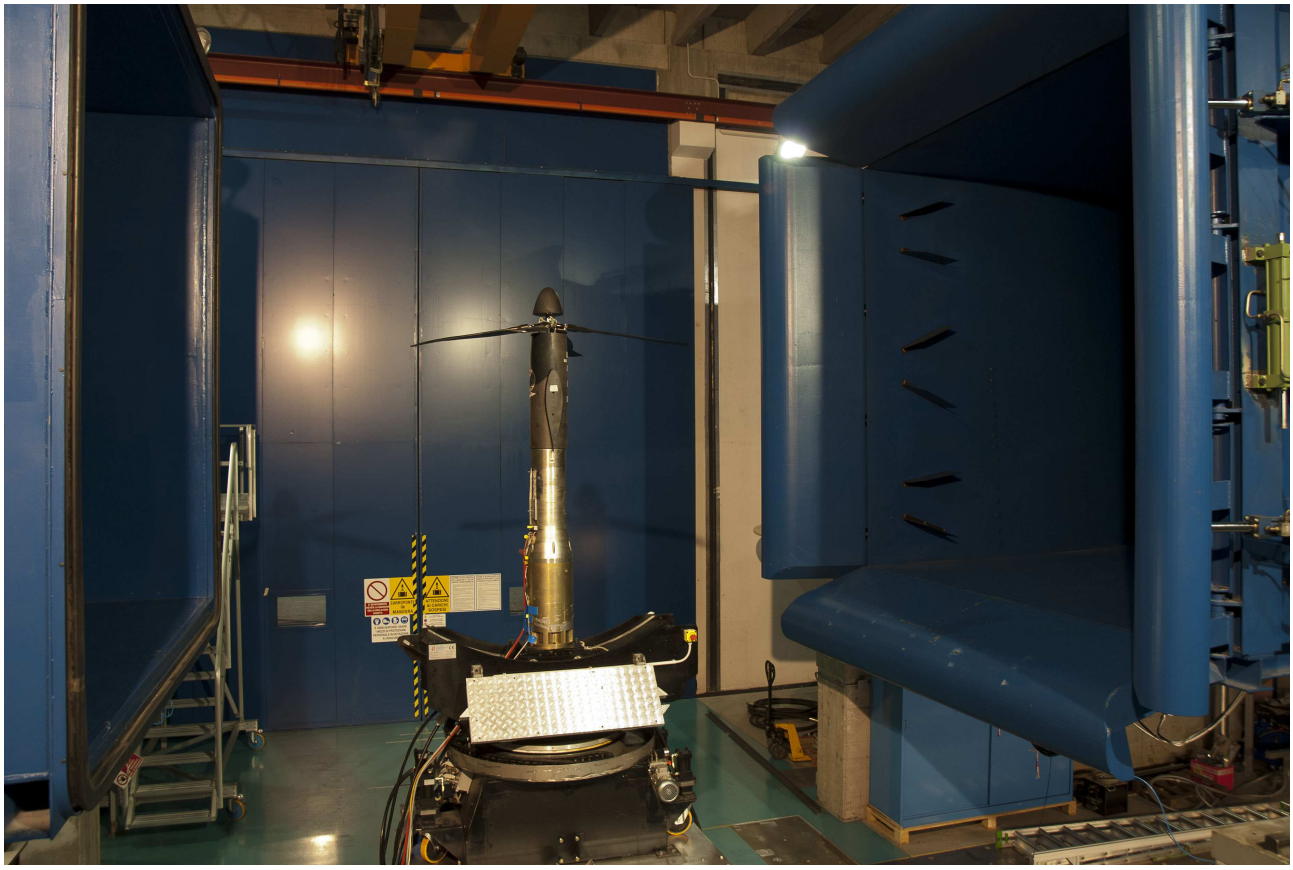

Figure 15: Isolated rotor test rig for hovering tests located inside the open test section of the Large Wind Tunnel of Politecnico di Milano.

numerical and experimental results validates the design methodology described in the present work.

5.3 Comparisons with reference proprotor

The publicly available data about other proprotors can be used to evaluate the quality of the obtained blade solution. Unfortunately these data are mainly related to the hovering condition while for the aeroplane mode only few data was published.

5.3.1 ERICA proprotor

A first design solution of the ERICA rotor blade was developed in the frame of the European project TILTrotor interactional AEROdynamics (TILTAERO [54]) and was then refined in the frame of European project Advanced European tiltrotor DYnamics and Noise (ADYN [14]). Both blade versions were tested in helicopter and aeroplane flight mode [15], the first one in the Large Low–speed Facility of the German–Dutch Wind Tunnel (DNW–LLF) and the second one in the Modane S1MA wind tunnel. However, only wind tunnel data for hovering tests was published in terms of absolute values.

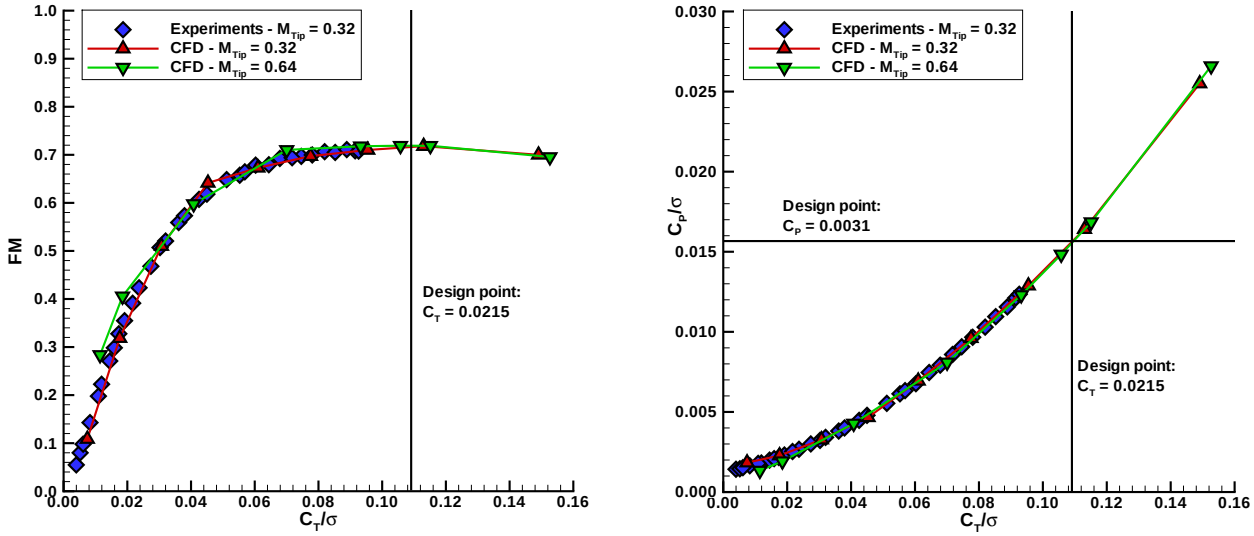

(a) (b)

Figure 16: Hovering rotor: comparison between experimental data and CFD calculations.

Note that the ERICA tiltwing tiltrotor was characterised by a four bladed, stiff in plane, homo-kinetic, gimballed rotor hub [13] which allowed for collective and cyclic pitch settings. The comparison between this data and the present solution is reported in Figure 17. As it can be seen, the present blade behaves better than the TILTAERO one but it is less efficient with respect to the ADYN blade. Unfortunately, as already mentioned, a comparison for the cruise condition is not possible in this case.

5.3.2 V–22 proprotor

The blade geometry of the V–22 Osprey tiltrotor was tested at the DNW–LLF in the frame of the Tilt Rotor Aeroacoustic Model (TRAM [55]) experimental program that was a key part of the NASA Short Haul Civil Tiltrotor (SHCT) project. The experiments were carried out by means of a 1/4–scale rotor model tested both in helicopter and aeroplane flight mode [56], the latter limited to low advance ratio. The comparison with the present solution is shown in Figure 17. As expected, the V–22 rotor, that is rather similar to a helicopter rotor, presented a better FM while the present solution resulted to be slightly more efficient in aeroplane mode if compared with the available V–22 data. Indeed, this second comparison is partially meaningful as both rotors were designed for higher cruise flight speed, but at higher $V/\Omega r$ the comparison is not possible due to the lack of published V–22 data. For the sake of completeness, the performance of the present blade at its design cruise forward speed is reported in the same figure. In this last case the propeller efficiency is lower with respect to low speed cases, as it might be expected, due to the Mach number effect [49]. On the other hand, it is noticeable

that for the design C_T/σ, the reduction in terms of propeller efficiency is negligible.

5.3.3 VDTR

The Sikorsky Variable–Diameter TiltRotor (VDTR [57]) concept was tested at the United Technologies Research Center Large Subsonic Wind Tunnel (UTRC–LSWT) by means of a 1/6–scale model. Also in this case the rotor was tested in both helicopter and aeroplane mode. However, some doubts arose about the consistency of the reported data for the aeroplane flight mode [58], so only the comparison in terms of FM is here presented. The hovering tests were carried out for two different rotor extensions (100 % and 83.3 % of the maximum rotor radius). As it can be seen from Figure 17, for both cases, the FM at $C_T/\sigma = 0.11$ (corresponding to the hovering design point for the present rotor) are quite close to each other and also quite close to the present result. However, at larger C_T/σ the VDTR rotor exhibited better performance particularly for the more extended rotor, as it might be expected.

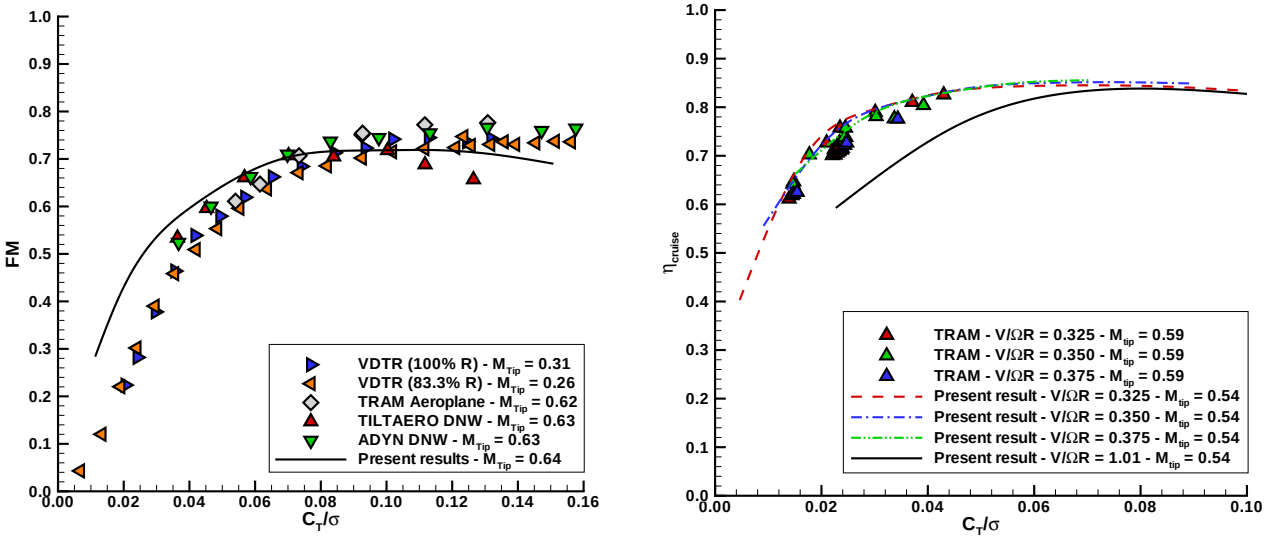

(a) Helicopter mode

(b) aeroplane mode

Figure 17: Proprotor performance: comparison with reference tiltrotor (ADYN and TILTAERO [15], TRAM [59] and VDTR [57]).

6 Conclusion

The present work describes the optimisation process adopted to design a new proprotor blade for a high–performance tiltwing tiltrotor aircraft. A two–level procedure was used for this purpose. The span–wise distributions of twist, chord and airfoil type were chosen in the first–level of the optimisation process by making use of a multi–objective genetic optimiser based on the NSGA–II algorithm and

combined with a classical BEMT solver. The individuals included in the Pareto–Optimal Front were analysed in order to select the individual showing the best compromise between helicopter and aeroplane performance and having, at the same time, a geometry suitable for manufacturing. Non–linear distributions of chord, twist and airfoil along the blade span were identified in this way. With the aim of reducing power losses due to onset of compressibility effects at the blade tip in cruise flight at high speed, the blade tip was refined in the second–level of the optimisation procedure. The non–linear sweep angle distribution along the blade span was then modified by moving the inner section of the blade ahead, in order to avoid stability and structural problems on the blade.

CFD calculations carried out with a 3D compressible Navier–Stokes code validated the predictions of the BEMT solver. Comparisons between CFD and BEMT calculations on the unswept blade showed very small differences, demonstrating that the BEMT solver used during the optimisation is suitable for this purpose. On the other hand, comparisons between swept and unswept blade by means of CFD illustrated important improvements in terms of performance both in helicopter and aeroplane flight mode. The effects of the sweep angle on the blade performance are evident both in hovering (anhedral effect) and in cruise (delay of compressibility losses). The good agreement showed by comparing CFD predictions and experiments carried out using a scaled rotor model in the Large Wind Tunnel of Politecnico di Milano validated CFD calculations.

The comparisons between the optimised proprotor blades and other rotor of reference tiltrotor aircraft (ERICA, V–22 Osprey and VDTR) demonstrated that the proposed optimisation procedure can be successfully adopted for the aerodynamic design of new proprotors. More in general, results suggest that the described procedure can be suitable for the design of helicopter rotors and aircraft propellers of all typologies.

References

[1] Foster, M., "The Future Evolution of the Tiltrotor," *AIAA/ICAS International Air and Symposium and Exposition: The Next 100 Years of Flight*, July 14–17 2003.

[2] Maisel, M., Giulianetti, D., and Dugan, D., "The history of the XV–15 tilt rotor research aircraft: from concept to flight," Monographs in Aerospace History, 17 SP–2000–4517, NASA History Division, Washington, D.C., USA, 2000.

[3] Snyder, D. E., "The Quad Tiltrotor: Its Beginning and Evolution," American Helicopter Society 56^{th} Annual Forum, Alexandria, VA, USA, May 2000, pp. 48–61.

[4] Gazdag, D. and Altonin, L., "Potential use of tiltrotor aricraft in Canadian aviation," Tech. Rep. TM–102245, NASA Technical Memorandum, Ames Research Center, Moffett Field, CA, USA, 1990.

[5] Reber, R., "Civil TiltRotor Transportation for the 21^{st} Century," *AIAA 93-4875*, AIAA International powered lift conference, 1993.

[6] Young, L., Lillie, D., McCluer, M., Yamauchi, G., and Derby, M., "Insights into Airframe Aerodynamics and Rotor-on-Wing Interactions from a 0.25–Scale Tiltrotor Wind Tunnel Model," American Helicopter Society Aerodynamics, Acoustics, and Test and Evaluation Technical Specialists' Meeting, San Francisco, CA, USA, January 23–25 2002.

[7] McVeigh, M. A., "The V–22 Tiltrotor Large–Scale Rotor Performance/Wing Download Test and Comparison With Theory," *Vertica*, Vol. 10, No. 3/4, 1986, pp. 281–297.

[8] Felker, F., "Wing Download Results from a Test of a 0.658-Scale V–22 Rotor and Wing," *Journal of the American Helicopter Society*, October 1992, pp. 58–63.

[9] McVeigh, M. A., Rosenstein, H. J., and McHugh, F. J., "Aerodynamic Design of the XV–15 Advanced Composite Tiltrotor Blade," American Helicopter Society Aerodynamics 39^{th} Annual Forum, St. Louis, MO, USA, May 9–11 1983.

[10] Paisley, D. J., "Rotor Aerodynamic Optimization for High Speed Tiltrotors," American Helicopter Society Aerodynamics 43^{th} Annual Forum, St. Louis, MO, USA, May 18–20 1987.

[11] Liu, J., Paisley, D. J., and Hirsh, J., "Tiltrotor Aerodynamic Blade Design by Numerical Optimization Method," American Helicopter Society Aerodynamics 46^{th} Annual Forum, Washington, D.C., USA, May 1990.

[12] Dancik, P., Mazzitelli, F., and Peck, W., "Test Experience on the Vertol 76 VTOL Research Aircraft," *American Helicopter Society* 14^{th} *Annual Forum*, April 16–19 1958.

[13] Alli, P., Nannoni, F., and Cicalè, M., "ERICA: The european tiltrotor design and critical technology projects," *AIAA/ICAS*, International Air and Space Symposium and Exposition: The Next 100 Years, Day-ton, Ohio, USA, July 14–17 2005.

[14] Lefebvre, T., Beaumier, P., Canard-Caruana, S., Pisoni, A., Pagano, A., Sorrentino, A., der Wall, B. V., Yin, J., Arzoumanian, C., Voutsinas, S., and Hermans, C., "Aerodynamic and aero-acoustic optimization of modern tilt-rotor blades within the ADYN project," *ECCOMAS*, 4^{th} European Congress on Computational Methods in Applied Sciences and Engineering, Jyväskylä, Finlande, July 24–28 2004.

[15] Beaumier, P., Decours, J., and Lefebvre, T., "Aerodynamic and Aeroacoustic Desing of Moder Tilt–Rotors: the Onera Experience," *ICAS*, 26^{th} International Congress of the Aeronautical Sciences, Anchorage, Alaska, USA, September 14–19 2008.

[16] Leishman, J. G. and Rosen, K. M., "Challenges in the Aerodynamic Optimization of High-Efficiency Proprotors," *Journal of the American Helicopter Society*, Vol. 56, No. 1, January 2011, pp. 12004–1200421.

[17] Brocklehurst, A. and Barakos, G. N., "A Review of Helicopter Rotor Blade Tip Shapes," *Progress in Aerospace Sciences*, Vol. 56, 2013, pp. 35–74.

[18] Liu, J. and McVeigh, M., "Design of Swept Blade Rotors for High Speed Tiltrotor Applications," *AIAA–91–3147*, AIAA Aircraft Design Systems and Operations Meeting, Baltimore, MD, USA, September 23–25 1991.

[19] Pape, A. L. and Beaumier, P., "Numerical Optimization of Helicopter Rotor Aerodynamic Performance in Hover," *Aerospace Science and Tecnology*, Vol. 9, No. 3, 2005, pp. 191–201.

[20] Servera, G., Beaumier, P., and Costes, M., "A weak coupling method between the dynamic code HOST and the 3D unsteady Euler code WAVES," *Aerospace Science and Tecnology*, Vol. 5, No. 6, 2001, pp. 397–408.

[21] Konak, A., Coit, D. W., and Smith, A. E., "Multi–Objective Optimization Using Genetic Algorithms: A Tutorial," *Reliability Engineering & System Safety*, Vol. 91, No. 9, 2006, pp. 992–1007, Special Issue – Genetic Algorithms and Reliability Special Issue – Genetic Algorithms and Reliability.

[22] Imiela, M., "High–Fidelity Optimization Framework for Helicopter Rotors," *Aerospace Science and Technology*, Vol. 23, No. 1, 2012, pp. 2–16.

[23] Deb, K., *Multi–objective optimization using evolutionary algorithms*, John Wiley and Sons Ltd, Southern Gate, Chichester, West Sussex, United Kingdom, 2008.

[24] Leusink, D., Alfano, D., Cinnella, P., and Robinet, J. C., "Aerodynamic rotor blade optimization at Eurocopter - A new way of industrial rotor blade design," *AIAA 2013-0779*, 51^{th} AIAA Aerospace Sciences Meeting including the New Horizons Forum and Aerospace Exposition, Grapevine, Texas, USA, January 7–10 2013.

[25] Johnson, C. S. and Barakos, G. N., "Optimising Aspects of Rotor Blades in Forward Flight," *AIAA–2011–1194*, 49^{th} AIAA Aerospace Sciences Meeting including the New Horizons Forum and Aerospace Exposition, Orlando, FL, USA, January 4–7 2011.

[26] León, E. R., Pape, A. L., Désidéri, J.-A., Alfano, D., and Costes, M., "Concurrent Aerodynamic Optimization of Rotor Blades Using a Nash Game Method," *American Helicopter Society* 69^{th} *Annual Forum*, May 21–23 2013.

[27] Wilke, G., "Variable Fidelity Optimization of Required Power of Rotor Blades: Investigation of Aerodynamic Models and their Application," 38^{th} European Rotorcraft Forum, Amsterdam, The Netherlands, September 4–7 2012.

[28] Droandi, G., Gibertini, G., and Biava, M., "Wing–Rotor Aerodynamic Interaction in Tiltrotor Aircraft," 38^{th} European Rotorcraft Forum, Amsterdam, The Netherlands, September 4–7 2012.

[29] Deb, K., "A fast and elitist multiobjective genetic algorithm: NSGA–II," *IEEE Transactions on Evolutionary Computation*, Vol. 6, No. 2, April 2002, pp. 182–197.

[30] Michalewicz, Z. and Janikow, C. Z., "Handling Constraints in Genetic Algorithms," Proceedings of the Fourth International Conference on Genetic Algorithms, 1991, pp. 151–157.

[31] Neubauer, A., "Adaptive Non–Uniform Mutation for Genetic Algorithms," *Computational Intelligence Theory and Application*, Vol. 1226, 1997, pp. pp. 24–34.

[32] Droandi and Gibertini, G., "Aerodynamic Blade Design With Multi-Objective Optimization For A Tiltrotor Aircraft," *Aircraft Engineering and Aerospace Technology*, Vol. 87, No. 1, 2015, pp. 19–29.

[33] Droandi, G., *Wing–Rotor Aerodynamic Interaction in Tiltrotor Aircraft*, Ph.D. thesis, Politecnico di Milano, 2014.

[34] MathWorks, T., "Global Optimization Toolbox, User's Giude," `http://mathworks.it`, 2013, [Online; accessed 20–December–2013].

[35] MathWorks, T., "Parallel Computing Toolbox, User's Giude," `http://mathworks.it`, 2013, [Online; accessed 20–December–2013].

[36] Johnson, W., *Helicopter Theory*, Princeton University Press, Princeton, New Jersey, USA, 1980.

[37] Leishman, J. G., *Principles of Helicopter Aerodynamics*, Cambridge Aerospace Series, New York, NY 10013–2473, USA, 2006.

[38] Gur, O. and Rosen, A., "Comparison between Blade-Element Models," *The Aeronautical Journal*, Vol. 112, No. 1138, December 2008, pp. 689–704.

[39] Goldstein, L., "On the Vortex Theory of Screw Propellers," *Proceedings of the Royal Society of London. Series A, Containing Papers of a Mathematical and Physical Character*, Vol. 123, No. 792, 1929, pp. 440–465.

[40] Abbott, I. and Doenhoff, A. V., *Theory of Wing Sections, Including a Summary of Airfoil Data*, McGraw–Hill Book Co., Inc. (Reprinted by Dover Publications, 1959), New York, 1949.

[41] Biava, M., Pisoni, A., Saporiti, A., and Vigevano, L., "Efficient rotor aerodynamics predictions with an Euler method," 29^{th} European Rotorcraft Forum, Friedrichshafen, Germany, September 16–18 2003.

[42] Spalart, P. and Allmaras, S., "One equation model for aerodynamic flows," *AIAA 92-0439*, 30^{th} AIAA Aerospace Science Meeting & Exhibit, Reno, Nevada, USA, January 6–9, 1992.

[43] Roe, P. L., "Approximate Riemann Solvers, Parameter Vectors and Difference Schemes," *Journal of Computational Physics*, Vol. 43, 1981, pp. 357–372.

[44] Venkatakrishnan, V., "On the accuracy of limiters and convergence to steady state solutions," *AIAA 1993–880*, 31^{st} AIAA Aerospace Science Meeting & Exhibit, Reno, Nevada, USA, 1993.

[45] Jameson, A., "Time Dependent Calculations Using Multigrid with Applications to Unsteady Flows past Airfoils and Wings," *AIAA 91–1596*, 10^{th} AIAA Computational Fluid Dynamics Conference, Honolulu, HI., 1991.

[46] Hirsch, C., *Numerical computation of internal and external flows*, John Wiley & Sons, 1988.

[47] Chesshire, G. and Henshaw, W. D., "Composite overlapping meshes for the solution of partial differential equations," *Journal of Computational Physics*, Vol. 90, 1990, pp. 1–64.

[48] Roskam, J., *Aircraft design*, Roskam Aviation and Engineering Corporation, Rt4, Box 274, Ottawa, Kansas, 66067, USA, 1985.

[49] Evans, A. and Liner, G., "A Wind–Tunnel Investigation of the Aerodynamic Characteristics of a Full–Scale Supersonic–Type Three–Blade Propeller at Mach numbers to 0.96," Tech. Rep. TR–1375, NACA, 1958.

[50] Favier, D., Ettaouil, A., and Maresca, C., "Numerical And Experimental Investigation Of Isolated Propeller Wakes In Axial Flight," *Journal of Aircraft*, Vol. 26, No. 9, 1989, pp. 837–846, American Institute of Aeronautics and Astronautics.

[51] Chae, S., Yee, K., Yang, C., Aoyama, T., Jeong, S., and Obayashi, S., "Helicopter Rotor Shape Optimization for the Improvement of Aeroacoustic Performance in Hover," *Journal of Aircraft*, Vol. 47, No. 5, 2010, pp. 1770–1783, American Institute of Aeronautics and Astronautics.

[52] Biava, M., *RANS computations of rotor/fuselage unsteady interactional aerodynamics*, Ph.D. thesis, Politecnico di Milano, Milano, Italy, 2007.

[53] Droandi, G., Zanotti, A., Gibertini, G., Grassi, D., and Campanardi, G., "Experimental Investigation of the Rotor–Wing Aerodynamic Interaction in a Titlwing Aircraft in Hover," *The Aeronautical Journal*, Vol. 119, No. 1215, May 2015, pp. 591–612.

[54] Visingardi, A., Khier, W., and Decours, J., "The Blind–Test Activity of TITLAERO Project for the Numerical Aerodyanmic Investigation of a Tilt Rotor," *ECCOMAS*, 4^{th} European Congress on Computational Methods in Applied Sciences and Engineering, Jyväskylä, Finlande, July 24–28 2004.

[55] Young, L. A., "Tilt Rotor Aeroacoustic Model (TRAM): A New Rotorcraft Research Facility," *American Helicopter Society International Specialist's Meeting on Advanced Rotorcraft Technology and Disaster Relief*, April 21–23 1998.

[56] Young, L. A., Jr., E. R. B., Yamauchi, G., and Botha, G., "Overview of the Testing of a Small–Scale Proprotor," *American Helicopter Society* 55^{th} *Annual Forum*, May 25–27 1999.

[57] Matuska, D., Dale, A., and Lorber, P., "Wind Tunnel Test of a Variable–Diameter (VDTR) Model," Tech. Rep. CR–177629, NASA, 1994.

[58] Stahlhut, C. and Leishman, J. G., "Aerodyanamic Design Optimization of Proprotors for Convertible–Rotor Concepts," *American Helicopter Society* 68^{th} *Annual Forum*, May 1–3 2012.

[59] Johnson, W., "Calculation of Tilt Rotor Aeroacoustic Model (TRAM DNW) Performance, Airloads, and Structural Loads," American Helicopter Society Aeromechanics Specialists' Meeting, Atlanta, Georgia, USA, November 2000.